Circuit-specific dendritic development in the piriform cortex

Laura Moreno-Velasquez[1], Malte Kaehne[2], Hung Lo[1], Stephen Lenzi[3], Jörg Breustedt[1], Dietmar Schmitz[1,4], Sten Rüdiger[3] and Friedrich W. Johenning[1#]

1. Neuroscience Research Center, Charité-Universitätsmedizin Berlin, Corporate member of Freie Universität Berlin, Humboldt-Universität zu Berlin, and Berlin Institute of Health
2. Institute of Physics, Humboldt Universität Berlin, Berlin, Germany
3. Sainsbury Wellcome Centre, University College London
4. NeuroCure Cluster of Excellence, Berlin, Germany

Corresponding author:

Friedrich Johenning
Neuroscience Research Center
CCO
Charitéplatz 1
10117 Berlin
Germany

Phone: ++49 30 450639336

Friedrich.johenning@charite.de

Running title: Piriform cortex dendrite development

Abstract

Dendritic geometry is largely determined during postnatal development and has a substantial impact on neural function. In sensory processing, postnatal development of the dendritic tree is affected by two dominant circuit motifs, ascending sensory feedforward inputs and descending and local recurrent connections. Two subtypes of layer 2 neurons in the three-layered anterior piriform cortex, layer 2a and layer 2b neurons, display a clear vertical segregation of these two circuit motifs. Here, we combined electrophysiology, detailed morphometry and Ca^{2+} imaging -both of neuronal networks as well as of subcellular structures-in acute mouse brain slices and modeling. This allowed us to compare the functional implications of distinct circuit-specific postnatal dendritic growth patterns in these two neuronal subtypes. We observed that determination of branching complexity, dendritic length increases and pruning occurred in distinct growth phases. Layer 2a and layer 2b neurons displayed growth phase specific developmental differences between their apical and basal dendritic trees. This was reflected by compartment-specific differences in Ca^{2+} signaling. The morphological and functional developmental pattern differences between layer 2a and layer 2b neurons dendrites provide further evidence that they constitute two functionally distinct streams of olfactory information processing.

Keywords
Piriform Cortex, brain development, dendrites, calcium signaling

Introduction

The complex geometry of neuronal dendritic trees in relation to their function is not yet fully understood. In sensory cortices, sensory input from the periphery is distributed to cortical neurons in an ascending sensory stream of input. Recurrent connectivity between cortical neurons constitutes the local and descending stream of input, which then transforms the sensory input into cortical output (Srinivasan and Stevens 2018; Kanari et al. 2019). Developmental growth patterns of dendritic structures are an important determinant of a neuron's function within the different circuits constituting its synaptic input space (Lanoue and Cooper 2018). This brings up the question of how dendritic morphology develops in relation to the two different glutamatergic circuit elements in sensory information processing, ascending sensory input and recurrent connectivity.

We investigated the palaeocortical three-layered anterior piriform or primary olfactory cortex (aPCx), which shares structural and functional similarities with the reptilian dorsal cortex (Fournier et al. 2015). The aPCx is the largest cortical region receiving olfactory sensory inputs. Peripheral odor information from nasal olfactory sensory neurons converges onto the aPCx via the olfactory bulb. Functionally, the aPCx synthesizes the segregated peripheral input into odor objects and identifies them (Wilson and Sullivan 2011). Unlike topographically organized neocortical sensory systems, afferent sensory and recurrent connectivity in the aPCx lack any apparent spatial structure and are therefore non-topographical (Srinivasan and Stevens 2018). Layer 2 is the main cellular layer of the olfactory cortex and harbors at least two types of glutamatergic neurons (Bekkers and Suzuki 2013). Based on the distribution of these glutamatergic projection neurons, layer 2 can be divided into layer 2a (superficial third) and layer 2b (deeper two-thirds). Layer 2a contains superficial so-called semilunar cells (layer 2a neurons). Layer 2b harbors pyramidal cells (layer 2b neurons) (Choy et al. 2015; Martin-Lopez et al. 2017). The two cell types display differences in functional circuit incorporation. Layer 2a neurons predominantly sample converging sensory input and distribute it unidirectionally to

the layer 2b and 3 neurons (Suzuki and Bekkers 2011; Choy et al. 2015). Layer 2b neurons receive sensory input and, in addition, are incorporated in a rich recurrent network (Suzuki and Bekkers 2011; Wiegand et al. 2011). Recently, it has been demonstrated in vivo that these two neuron types play different roles in reading out converging sensory input and performing pattern storage and completion via recurrent circuits (Bolding et al. 2019). This vertical organization of input space of layer 2 neurons extends to the dendritic tree, where sensory and recurrent functional domains are spatially segregated. In the apical dendrites of all neurons in layer 2, the majority of sensory input projects to the superficial layer 1a. Layer 1a can be clearly distinguished from layer 1b, which, together with inputs in layer 2 and 3, samples recurrent inputs (Franks and Isaacson 2005; Johenning et al. 2009). In aPCx, we therefore observe a clear vertical segregation of functionally distinct cell types and of different functional dendritic domains. This feature of aPCx makes layer 2 of the aPCx an ideal model for the differential analysis of dendritic growth patterns related to sensory input and recurrent connectivity.

Here, we studied developmental mechanisms of dendritic growth in layer 2a and layer 2b neurons in acute brain slices of the aPCx. We applied electrophysiology, detailed morphometry of 3D-reconstructed neurons, subcellular and population Ca^{2+} imaging and computational modelling. We identified distinct developmental dendritic growth patterns. Ca^{2+} signaling plays a central role in shaping dendritic growth in relation to neuronal activity (Konur and Ghosh 2005). We could distinguish compartment-specific growth pattern related differences in Ca^{2+} signaling in layer 2a and layer 2b neurons. Using modeling, we were able to relate differences in dendritic integration to concentration-variant and -invariant identity coding of odors in different cell populations. We interpreted the distinct developmental patterns described here as a strategy for generating parallel streams of olfactory information processing in a palaeocortical structure. This enabled us to identify evolutionary conserved mechanisms that may drive circuit-specific dendritic growth in a non-topographic sensory system.

Materials and Methods

Slice preparation

Acute brain slices were prepared from C57Bl6N mice except for population Ca^{2+} imaging experiments with GCaMP (Fig. 4), where Ai95-NexCre mice were used. In experiments for Figs. 1-6, the horizontal slicing orientation was chosen because it best preserves rostrocaudal association fibers (Demir et al. 2001). For dendritic spike measurements in Fig. 7, we used coronal slices. All procedures were in accordance with the national and institutional guidelines and approved by the local health authority and the local ethics committee (Landesamt für Gesundheit und Soziales, Berlin; animal license number T100/03). For electrophysiological characterization and morphological reconstruction, acute brain slices were prepared at 4 age intervals: p1-2, p6-8, p12-14 and p30-40. For measurements of NMDA-spikes, coronal slices were prepared at p14-21. Brains from p30-40 mice and from mice used for dendritic spike measurements were prepared in ice-cold artificial cerebrospinal fluid (ACSF; pH 7.4) containing (in mM): 87 NaCl, 26 $NaHCO_3$, 10 Glucose, 2.5 KCl, 3 $MgCl_2$, 1.25 NaH_2PO_4, 0.5 $CaCl_2$ and 50 sucrose. Slices were cut at 400 µm thickness, and incubated at 35°C for 30 min. The slices were then transferred to standard ACSF containing (in mM): 119 NaCl, 26 $NaHCO_3$, 10 Glucose, 2.5 KCl, 2.5 $CaCl_2$, 1.3 $MgCl_2$, and 1 NaH_2PO_4. Slices from other age groups were cut in ice-cold standard ACSF and incubated for 30 min in standard ACSF at 35°C. The slices were then stored in standard ACSF at room temperature in a submerged chamber for 0.5–6 h before being transferred to the recording chamber. For dendritic spike measurements in Fig. 7, 1 µM of Gabazine was added to the recording solution. For dendritic Ca^{2+} imaging during spontaneous network activity (Fig. 5), slices were prepared between p4 and p8. For population Ca^{2+} imaging (Fig. 4), the age range was p0 to p13. Both experiments requiring spontaneous network activity were prepared in ice-cold ACSF containing (in mM): 125 NaCL, 25 NaCHCO3, 10 Glucose, 4 KCL, 1.25 NaH2PO4, 2 CaCl2, 1 MgCl2. Slices were incubated at 35°C for 30 min and stored at room temperature in a submerged chamber for 0.5–7 h. All

recordings were performed at near-physiological temperature (32-34 °C)

Electrophysiology

Whole-cell current clamp experiments were performed at near physiological temperature (32-34 °C) using an Axon Multiclamp 700B amplifier (Molecular Devices, Sunnydale, CA, US). For morphological reconstruction and characterization, signals were low pass filtered at 2 kHz and digitized at a sampling rate of 20 kHz (BNC-2090, National Instruments Corporation, Austin, Tx, US). Pipettes (3-6 MΩ) were filled with an intracellular solution containing (in mM): 135 K-gluconate, 6 KCl, 10 HEPES, 0.2 EGTA, 2 $MgCl_2$, 2 Na-ATP, 0.5 Na-GTP, 5 phosphocreatine Na (pH: 7.3) and Biocytine (0.20%). Liquid junction potential (LJP) was not corrected. Bridge balance compensation was applied in current clamp. Cells were discarded if the resting membrane potential was above -55 mV or the series resistance exceeded 30 MΩ. For dendritic spike recordings, signals were low pass filtered at 8 kHz and digitized at a sampling rate of 20 kHz. Pipettes (3-6 MΩ) were filled with an intracellular solution containing (in mM): 130 K-gluconate, 20 KCl, 10 HEPES, 4 MgATP, 0.3 NaGTP and 10 phosphocreatine (pH:7.3, adjusted with KOH), 30 µM Alexa 594 and 500 µM fluo-5F. Experiments were conducted without exceeding -200 pA at resting membrane potential (Layer 2a neurons were held at -60 mV, and layer 2b neurons were held at -70 mV). Series resistance was below 30 MΩ. After dye-filling the patched neuron for 10 mins, we placed the theta glass stimulation electrode close to the distal dendrite in layer 1a of the piriform cortex. Stimulation protocol was set to 3 pulses at 50 Hz with 10 µA steps (with one exception in layer 2b neuron, which was with 20 µA steps.).

Electrophysiological Analysis

Analysis was performed using custom-written routines in Python. Resting membrane potential (Vm) was taken as the mean value of the baseline before current injections were performed.

Input resistance (IR), membrane time constant (Tau) and membrane capacitance (Cm) were calculated from the voltage response to an 80 pA hyperpolarizing current step. Action potential (AP) threshold was defined as the membrane potential at the point where the slope (dV/dt) reached 1 % of its maximum. The fast after-hyperpolarisation (fAHP) was defined as the difference between AP threshold and the minimum voltage seen immediately after the AP peak (within 5 ms). Finally, the burst index was calculated as the ratio between Δt4 and Δt1. Δt1 is the time interval between the first and second AP, and Δt4 is the interval between the fourth and fifth AP. For comparability, these values were extracted from the first 600 ms current injection step that elicited at least 9 APs. When analyzing the integrative behavior of apical dendrites in Fig. 7, we analyzed the changes in EPSP size upon linear increase of stimulation intensity. To quantify EPSP size, we measured the amplitude and area under curve of a 60 ms time window following the 3rd pulse compared to baseline (50 ms period before stimulus). Effects of APV were quantified for the largest response that did not yet evoke an AP.

Immunohistochemistry

Slices with biocytin-filled cells were stored in 4 % paraformaldehyde (PFA) overnight. The following day, slices were washed 3 times (10 mins each) in PBS and incubated in a blocking solution composed of 5 % normal goat serum (NGS, Biozol), 1 % Triton-X (Sigma) and PBS, for 3 hours at room temperature with gentle agitation. Primary antibodies were diluted in blocking solution (2.5 % NGS, 1 % Triton-X, PBS) and slices were incubated for 72 hours at 4 °C. Biocytin-filled neurons were labeled with a streptavidin marker conjugated to Alexa Fluor (AF) 488 (Invitrogen, S-32354; 1:500 dilution). Additionally, the LOT and mitral cell axons in layer 1a were labeled with calretinin (anti-mouse; Millipore, MAB1568; 1:1000 dilution or anti-rabbit; SWANT, 7697; 1:4000 dilution) and interneurons with GAD 67 (anti-mouse; Millipore, MAB 5406; 1:500 dilution), GAD 65/67 (anti-rabbit; Chemicon, AB 11070; 1:500 dilution) or Gephyrin (anti-mouse; SYSY 147 111; 1:500 dilution).

Following this, slices were washed 2 times (10 mins each) with PBS and secondary antibodies (goat anti-rabbit AF 555, goat anti-rabbit AF 647, goat anti-mouse AF 555, goat anti-mouse AF 647; Invitrogen; 1:500 dilution in 0.5% Triton, PBS) were applied for 3 hours at room temperature. Finally, slices were washed 3 times (10 mins each) in PBS and mounted on glass slides in mounting medium Fluoroshield with 4', 6-diamidino-2-phenylindole (DAPI; Sigma).

Reconstructions and Morphological Analysis

Mounted slices were visualized on a fluorescent microscope (10x objective, 0.3N.A.; Leica) in order to identify and select the biocytin-filled neurons located in the aPCx for further reconstruction. Only neurons that displayed homogenous filling with Biocytin and lacked obvious amputation of the dendritic tree by slicing were analyzed. Therefore, not all neurons chosen for electrophysiology were also chosen for morphological reconstruction and vice versa. Selected slices were then imaged on an upright Leica TCS SP5 confocal microscope (Leica Microsystems) through a 20x immersion objective (0.7 N.A.; Leica) with 405 nm (diode), 488 nm (Argon laser), 568 nm (solid state) and 633 nm (Helium, Neon) laser lines. For biocytin-filled neurons, the perisomatic field of view was further imaged through a 63x immersion objective (1.4 N.A.; Leica) to validate the spine density. Cells were selected and classified according to their position in layer 2 of the anterior piriform cortex using FIJI (https://imagej.nih.gov/ij/). The position in layer 2 was defined as the smallest distance from the soma to the border between layer 1b and layer 2a, normalized to the total width of layer 2 for each neuron. The border between layer Ia and Ib was similarly traced to later classify the apical dendrites according to their synaptic inputs. Neuronal morphologies were then reconstructed with neuTube software (Feng et al. 2015) and exported as SWC files. Morphometric parameters were extracted with L-measure software (Scorcioni et al. 2008) and analysed with R studio and Python using btmorph v2 (Torben-Nielsen 2014) and scipy packages.

Ca^{2+} Imaging

For population Ca^{2+} imaging of neonatal spontaneous synchronous network events (Fig. 4), we used the genetically encoded Ca^{2+} indicator (GECI) GCaMP6F. NEX-Cre mice (Goebbels et al. 2006) were crossed with Ai95 animals (https://www.jax.org/strain/024105(Madisen et al. 2015)) for constitutive GCaMP6F expression in excitatory cells only. For imaging average population activity in rectangular ROIs, we pooled the GCaMP data with data from slices bolus-loaded with synthetic dye. For bolus loading, we stained the tissue with a solution containing 50 µg Oregon Green 488 BAPTA-1AM (OGB1-AM), 38µl Hepes-buffered ringer and 2µl of 20% weight per volume pluronic in DMSO. This solution was applied by micropipette pressure ejection (2-5µm tip, 40-80mbar, 5-7 minutes) adapted from a similar approach (Wiegand et al., 2011). Dye was applied to the surface of ~400 x 400µm of layer II piriform cortex. Recordings were taken after at least 25 minutes had been allowed for the AM-dye to be internalized and processed by the neurons.

When analyzing dendritic Ca^{2+} signals during the first postnatal week (Fig. 5), we opted for dye delivery by electroporation to minimize disturbances of the intracellular milieu (Lang et al. 2006; Nevian and Helmchen 2007). Electroporation pipettes were filled with 1mM Oregon-Green BAPTA-1 (OGB1) and 150 µM Alexa 594 dissolved in ddH2O. The single 10V electroporation pulse lasted 10 ms.

For all experiments involving spontaneous network activity, Ca^{2+} imaging was performed using a Yokogawa CSU-22 spinning disc microscope at 5000rpm. The spinning disc confocal permitted the generation of a large field of view time series at a high acquisition rate. A 488 nm Laser was focused onto the field of view using a 40x objective. Emission light was filtered using a 515±15nm bandpass filter. Fluorescence was detected using an Andor Ixon DU-897D back-illuminated CCD, with a pixel size of 16µm. Andor iQ software was used for data acquisition. Population Ca^{2+} imaging was performed at 10 Hz when single cells were measured. For

pharmacological experiments with gabazine, we recorded at 40 Hz using 2x2 binning. For dendritic imaging, acquisition of 4 z-frames separated by 3 to 5 µm was enabled by a piezo stepper (P726 PIFOC, Physik Instrumente, Karlsruhe, Germany) incorporated between the microscope and the objective. For these experiments, image acquisition was performed using 2x2 binning and the temporal resolution of the z-frames was around 20 Hz. For evoked global events, a stimulation electrode was placed in layer 3 under the neurons of interest. Stimulation was performed by delivering 10 stimuli at 20 Hz, stimulation intensity was in the range between 200 and 2000 µA.

For analysing dendritic spikes using 2P-imaging, 30 µM Alexa-594 and 500 µM Fluo-5F were added to the intracellular solution. A Femto 2D two-photon laser scanning system (Femtonics Ltd., Budapest, Hungary) equipped with a femtosecond pulsed Ti:Sapphire laser tuned to λ=805 nm (Cameleon, Coherent, Santa Clara, CA, US) controlled by the Matlab-based MES software package (Femtonics Ltd., Budapest, Hungary) was used. Fluorescence was detected in epifluorescence mode with a water immersion objective (LUMPLFL 60x/1.0 NA, Olympus, Hamburg, Germany). Transfluorescence and transmitted infra-red light were detected using an oil immersion condenser (Olympus). The average scanning speed was 300 Hz and the intermediate sections were jumped over within 60 µs using a spline interpolated path. Dendritic Ca^{2+} transients were measured every 30 s.

Imaging Analysis

For population Ca^{2+} imaging (Fig. 4), FOVs with at least 5 minutes of recordings were included in the analysis. Videos were motion corrected using Suite2p (Pachitariu et al. 2016) and analysed using custom python code and SamuROI (Rueckl et al. 2017). If motion artefacts were too great to be corrected they were not included in the subsequent analysis. Each pixel of the raw data was normalised using the 6-sample window with the lowest standard deviation. Traces were

extracted from each ROI and event detection was carried out using standard peak detection algorithms in python, applied to 60s blocks of the data and manually curated.

The upper and lower boundaries of layer 2 were manually defined based on cell density. For detection of global events, we measured the average change in fluorescence for all pixels of layer 2 piriform cortex, including the neuropil, using a rectangular ROI defined by the upper and lower boundaries of layer 2.

For single cell analysis we used a semi-automated method outlined in SamuROI based on image segmentation with Ilastik (Sommer et al. 2011). This was required because a large number of cells were inactive, or closely packed and/or synchronous in their activity. Ilastik was trained to segment z-projection sum images of a subset of FOVs to produce a 5-label image (nuclei, somata, bright debris, dark debris and background). Cells were detected using the nuclei label with false positives manually rejected. Using these cell locations, the somata image was divided into territories using watershed segmentation and only the nearest pixels to each nucleus were included. ROIs with fewer than 70 pixels were rejected. We calculated the $\Delta F/F$ for each ROI and subtracted an estimate of the local neuropil contribution using an equal number of randomly selected non-cell pixels within a fixed radius of 70 pixels.

For pharmacological experiments the 5 minutes of recording preceding drug wash in was compared with 5 min of recording 10 minutes after wash in.

For measuring spontaneous dendritic activity (Fig. 5), Ca^{2+}-induced fluorescence changes were calculated as $\Delta F/F$ values. The minimal length of a dendritic segment for hotspot analysis was 9.6 µm, which corresponds to six 1.6 µm segments of our analysis raster (Fig. 5A1). To account for global activity, we first subtracted the median amplitude of all segment Ca^{2+} transients in a dendritic branch or subbranch. We only included dendrites in which we could detect individual segment traces larger than 2 SDs of their pre-event baseline noise. Dendrites with missing segments in the 3D-time lapse recording were excluded. Peaks were analyzed using the PeakUtils package in python, with an interpeak distance of at least 3 segments. The z-score of

a peak based on the variability of the peaks of a given segments is a good indicator of the prominence and amplitude of a hotspot in relation to its surrounding. We chose this z-score measure to quantify hotspots because intercellular loading differences and inter-event differences in signal amplitude (which can be substantial based on the spontaneous nature of the events we investigate here) affect the measure less than e.g. fluorescence peak-based analysis. When hotspots appeared in the same dendritic segment in several events, their values were averaged. For global events mimicking spontaneous dendritic activity evoked by extracellular stimulation, we performed analysis on the peak ΔF/F signal using the same 1.6 µm spaced analysis raster. Here, stimulus-locked peak ΔF/F signals in a subsegment were averaged from all sweeps if a hotspot was detected in any pre or post sweep. Peaks were detected in a tolerance window of ± 1 subsegments in consecutive sweeps.

For measuring the amplitude of EPSP/dendritic spike -related dendritic Ca^{2+} transients using two-photon imaging (Fig. 7), we calculated the ΔG/R ratio as described in (Johenning et al. 2015). Amplitudes were measured as the averaged ΔG/R value the first 130ms after the second synaptic stimulus and are averages of 3 sweeps. Amplitude measurements were performed under the maximal response ROI right under the stimulation electrode. Effects of APV were quantified for the largest response that did not yet evoke an AP.

Modelling:

For the model in Fig. 6, we assumed that the density of synapses on the branches of a dendrite is constant, i.e. depends linearly on the length of a branch. We assumed that upon odor exposure a maximum of 70 active synapses can arrive at a single neuronal dendrite. Following recent experimental measurements (Srinivasan and Stevens 2018), we considered 3700 glomeruli, 9.7×10^7 synapses between all glomeruli and all layer 2 neurons and a total of 41000 layer 2 neurons. Hence, we dealt with an average 9.7×10^7 / 41000 = 2366 synapses between all glomeruli and one neuron. Thus for 70 synapses to be activated upon odor exposure, we

assumed that 109 glomeruli are activated per odor (=3700x70/2366).

We characterized the morphology of a neuron through its mean branch length (BL), which we found to range from 40 to 110 µm (mean is 72 µm), cf. Results. The total dendritic branch length on average is approximately 1800 µm.

For simplicity, we approximated the length of any branch by the mean values of the respective neurons. Accordingly, dendrites could have a maximum of 1800/40 = 45 and a minimum of 1800/110 = 16 branches.

We distinguished the two cases of clustered and distributed stimulation. We assumed that a neuron fires if it is exposed to more than n_{dist}=40 active input synapses or n_{clus}=10 active inputs arriving on the same branch. The excitation behavior is schematically illustrated in Figure 6 H1, showing a simplified version of the non-linear dendritic integration scheme proposed by Poirazi et al. (Poirazi et al. 2003). Specifically, we considered every neuron as a two-layered network that may or may not produce a network response (express a somatic action potential) to a presented stimulus set. This response is triggered in cases when the distributed input reaches a certain threshold number (reflecting a number of active input synapses), which can be understood as a linear integration scheme of the neuron. In addition, the network may produce a response to a dendritic spike. In our model, dendritic spike led to the non-linear integration of synaptic input, which is mimicked through the activation gates on every branch of the neuron (first layer of the network). In figure 6H1, this first layer of the network is shown as blue circles. The green circle represents the soma. The magnification insets illustrate the stimulus response relationship of the separate branches and the soma, respectively. The model was constructed such that a somatic response is expressed, if the distributed stimulation crosses the threshold value n_{dist}, or if one of the branches expresses a dendritic spike, which relates to the number of active synapses on the branch crossing the threshold number of clustered stimulation n_{clus}.

Using this described model, we investigated the additional response probability that is introduced through considering clustered stimulation. We supposed the number of odor-

activated synapses (which we refer to as λ) connected to a given neuron to be random. The probability of finding a neuron that is connected to n or more odor activated synapses can then be approximated as

Eq. (1)

$$P(\lambda, n) = 1 - \sum_{k=1}^{n-1} \frac{\lambda^k \mathrm{e}^{-\lambda}}{k!}$$

Eq. (1) allowed us to map the response probability of a neuron to a presented stimulus. In the case of clustered stimulation, this picture is slightly different: Instead of the mean number of synapses per neuron, the mean number of synapses per branch is the relevant quantity. The mean number of branches (NB) is approximately the total dendritic branch length (TDBL) divided by the mean branch length (BL). We took the distribution of BL into account as we reasoned that longer branches optimize the input-output relationship in case of clustered stimulation. At P12-14, the length of the dendritic branches ranged from 40 µm to 110 µm. The response probability for clustered stimulation is modeled as:

Eq. (2)

$$P(\lambda, n) = 1 - \left(1 - \sum_{k=1}^{n-1} \frac{\lambda^k \mathrm{e}^{-\lambda}}{k!}\right)^{\frac{\mathrm{TDBL}}{\mathrm{BL}}}, \quad \text{with} \quad \lambda = S \cdot \frac{\mathrm{BL}}{\mathrm{TDBL}}$$

It is important to note that under such a scheme, stimulation of any dendritic branch can be sufficient to excite the neuron.

For Fig. 8, we employed the integrate-and-fire-or-burst neuron model to study the response behavior of a neurons to an input spike train. For a detailed description of the model refer e.g. to (Smith et al. 2000; Casti et al. 2002). It is a two-dimensional model for the membrane potential and a calcium conductance variable, with an additional discontinuous reset for the membrane potential.

The dynamics of the membrane potential read:

$$C\dot{V}(t) = I - g_L(V - V_L) - g_T m_\infty h(V - V_T)$$

where V_L and V_T are reversal potentials of leakage and calcium ions, respectively, (g_L and g_T are corresponding conductance constants). m_∞ represents an activation function for the Ca2+, which is modeled as

$$m_\infty = H(V - V_h)$$

where $H(x)$ is the Heaviside step-function, which is zero if $x < 0$ and one otherwise.

h represents the calcium conductance variable, with:

$$\dot{h} = -\frac{h}{\tau_h^-} H(V - V_h) + \frac{1 - h}{\tau_h^+} H(V_h - V).$$

The parameter V_h divides the V-axis into a hyperpolarizing region ($V < V_h$), where the calcium current is deinactivated, and a nonhyperpolarizing region ($V > V_h$) in which the calcium current is inactivated. The timescale τ_h^- sets the duration of the burst and τ_h^+ sets the inactivation rate. The time course of this intrinsic parameter approximates hyperpolarizing synaptic input from feedback interneurons that terminates neuronal hyperpolarization in the aPCx (Stern et al. 2018).

Whenever the voltage reaches a threshold value V_{thres} it is reset to the reset potential V_{r}.

For our simulations we used the following parameter:

C = 2 µF/cm^2

V_L = -65 mV, g_L = 0.035 mS/cm^2

V_T = 80 mV, g_T = 0.07 mS/cm^2

V_r = -50 mV, V_{thres} = -35 mV,

V_h = -60 mV, τ_h^- = 30 ms, τ_h^+ = 10 ms

Compared to the model as described by (Smith et al. 2000), V_T was reduced (from 120mV) in order to decrease the interspike interval during a burst. Secondly the timescales were adjusted such that a burst initiates roughly after about 50 ms in case of stimulation with 100 Hz input spike rate (originally: τ_h^- = 100 ms, τ_h^+ = 20 ms) and expresses about 5-6 spikes during its course.

Similar to the study of (Casti et al. 2002), we considered synaptic input in form of pre-synaptic input spike trains, but considered the synaptic current to be $I = g(V)\Delta V$. We considered a membrane potential increment of ΔV=2 mV. We compared the simulation results of two different versions of the model, which can be distinguished by their functional dependence of the synaptic conductance on the neurons membrane potential. In the case of a constant conductance ($g(V) = 1$) we referred to the model as linear integrate-and-fire-and-burst (IFB) neuron. For the nonlinear version of the model neuron (non-linear IFB), we considered a synaptic conductance of

$$g(V) = \frac{2}{1 + \exp(-0.5(V + 65))}.$$

Response rates were calculated as the inverse of the interspike intervals for a certain time. They resulted as the sum of the inverse of all registered interspike intervals, divided by the number of all considered neurons (here 5000) for each input rate and neuron type (linear and non-linear IFB). Note that this is the reason for the slow onset of the population response, which may not be confused with a slow (low rate) onset of firing of an individual neuron.

Statistics

Data were first tested for normality. Statistical tests were performed as indicated. We used the paired and unpaired t-test, Wilcoxon signed rank test, Mann-Whitney test, one-way ANOVA with Holm-Sidak's multiple comparisons test or Kruskal–Wallis test with Dunn's multiple comparison as a post hoc test as indicated in the figure legends. Additionally, spearman correlation test was used to measure the association between cell position and branch-length in figure 3D and the association between the effect of gabazine and postnatal age in figure 4C. Numerical values are given as mean and SEM unless otherwise stated.

Results

Layer identification in postnatal development

In acute horizontal mouse brain slices we performed whole cell patch clamp recordings of randomly sampled excitatory neurons in layer 2a and layer 2b. Excitatory neurons were distinguished from interneurons by at least one of the 3 criteria: firing profile (Suzuki and Bekkers 2010), morphology and a negative post-hoc staining for interneuron markers. During patching, neurons were filled with biocytin for later morphological reconstructions (Fig. 1A1). Layer 2 can be divided into layer 2a (upper third) and layer 2b (deep two-thirds) (Choy et al. 2015; Martin-Lopez et al. 2017). For analysis, the extent of layer 2 was delineated using a DAPI stain (Fig. 1A2). We confirmed the location of the aPCx, which is especially challenging in the postnatal day (p) 1-2 and p6-8 group, by staining the LOT and layer 1a fibers with calretinin (Sarma et al. 2011; Fig. 1A3). The calretinin staining also permitted clear delineation of dendritic segments terminating in layer 1a (Fig, 1A4, see Fig. 6). 3D reconstructions using neutube (Feng et al. 2015) of layer 2a (Fig.1B1; n=46/25 neurons/ mice) and layer 2b (Fig.1B2; n=43/27 neurons/mice) neurons were analyzed at four time windows: Right after birth (p1-2, layer 2a: n=6/4; layer 2b: n=12/6; neurons/ mice), at the end of the first postnatal week (p6-8, layer 2a: n=10/5; layer 2b: n=10/7; neurons/ mice), during the critical period of heightened sensory synaptic and structural plasticity (Franks and Isaacson 2005; Poo and Isaacson 2007; p12-14, layer 2a: n=11/8; layer 2b: n=9/8; neurons/mice) and after the critical period (>p30,

layer 2a: n=19/6; layer 2b: n=12/6; neurons/mice; Fig. 1B).

Figure 1

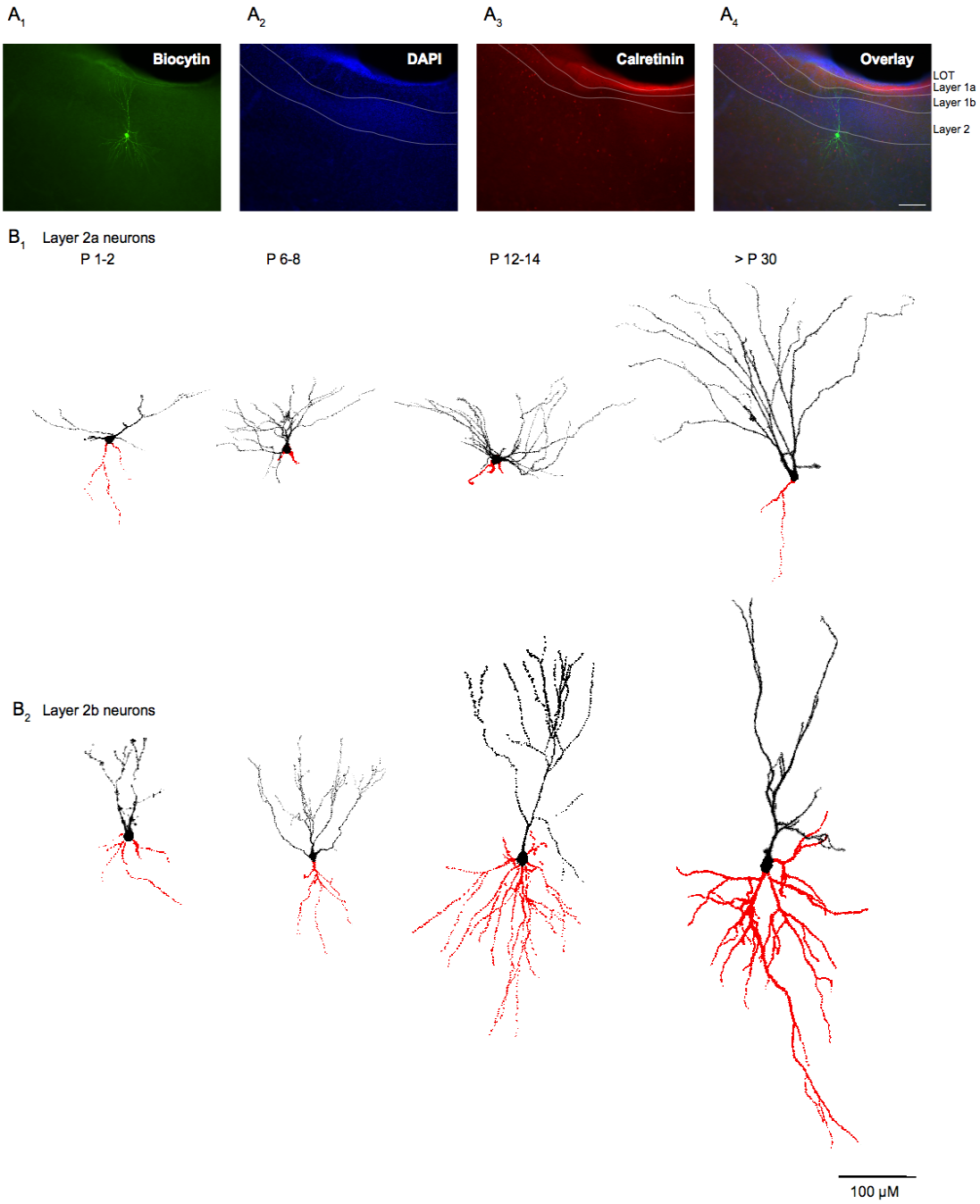

Figure 1

Localization and differentiation of the two principle neurons in Layer 2 of the aPCx

(A) Slice containing one recorded neuron filled with biocytin (A1) and additionally, post hoc labelled with DAPI (A2) and calretinin (A3). The overlay (A4) shows the recorded neuron located in Layer 2b of the aPCx. (B) 3D Morphological reconstructions of different layer 2a (B1) and layer 2b (B2) neurons at four time windows: Right

after birth (p1-2), at the end of the first postnatal week (p6-8), at the end of the second postnatal week (p12-14) and after the fifth postnatal week (>p30). Soma and apical dendrites are in black and basal dendrites in red. Scalebar 100 µm.

Electrophysiological and morphological differences between layer 2a and layer 2b neurons

Electrophysiological characterization was performed for a subset of neurons at p12-14 (layer 2a: n=10/6; layer 2b: n=9/7; (neurons, mice)) and at >p30 (layer 2a: n=14/7; layer 2b: n=11/6; (neurons, mice)). When sampling the whole extent of layer 2a and layer 2b, we did not find consistent electrophysiological differences between the two cell types at both ages. Of all our age groups, our p12-14 data most closely matches the p13-p30 observation window used for the initial description of electrophysiological differences between superficial and deep layer 2 neurons in a mouse strain closely related to ours (Suzuki and Bekkers 2006). While we found a similar trend regarding the difference in input resistance, our cell population displayed less pronounced differences in burstiness, resting potential, membrane time constant, membrane capacitance and AP threshold (Table 1). This may be due to differences in sampling (covering the whole extent of layer 2 in our case rather than focusing on the lower layer 2/3 and upper border as has been done previously) and changes in intrinsic electrical properties when using a KMESO4-based intracellular solution as opposed to a KGLUC-based intracellular solution in our case (Kaczorowski et al. 2007).

In addition to previously reported electrophysiological differences, the less complex basal dendritic tree of superficial layer 2a cells compared to deeper neurons in layer 2b is a prominent distinctive feature (Bekkers and Suzuki 2013). After the first postnatal week, we saw clear differences in the architecture of the basal dendritic tree between layer 2a neurons and layer 2b neurons. As expected, the number of basal branches and the total dendritic branch length were significantly smaller in layer 2a than in layer 2b neurons at all ages examined (Figs. 3A2 and 3). When plotting the normalized cell depth in layer 2 against the total dendritic branch length of

each neuron's basal tree, we saw a clear correlation at all developmental stages (Fig. 3D). We observed a stable superficial to deep gradient of basal dendritic tree length and complexity over postnatal development. Using cell depth as a classification parameter, morphological differences in the basal dendritic tree permitted us to distinguish between two broad cell classes.

	12-14 pd		>30 pd		
	SL	SP	SL	SP	
Vm (mV)	-75.32 ± 1.96	-71.77 ± 3.05	-71.88 ± 1.89	-69.60 ± 2.40	
Rin (MΩ)	233.35 ± 40.24	143.12 ± 24.27	168.71 ± 22.65	207.03 ± 45.94	
Tau (ms)	25.65 ± 2.94	22.35 ± 3.79	20.79 ± 1.98	21.49 ± 1.39	
Cm (pF)	123.17 ± 11.86	156.69 ± 9.21	135.89 ± 9.66	134.90 ± 18.22	
Threshold (mV)	-35.97 ± 1.50	-39.88 ± 1.15	-40.28 ± 1.52	-41.44 ± 1.18	
FAHP (mV)	7.75 ± 1.30	5.11 ± 1.44	10.83 ± 1.59	8.01 ± 0.68	
Burst Index	1.60 (0.95-17.85)	1.75 (1.14-13.17)	2.28 (1.18-35.04)	2.93 (1.28-14.87)	median (range)

Distinct growth phases in apical and basal dendrites

We chose a set of morphometric parameters to describe the growth of the apical (Fig. 2) and basal (Fig. 3) dendritic tree: number of branches, total dendritic branch length, number of stems, average individual branch length and branch density as a function of distance from the soma. Using these parameters we defined three distinct growth phases. In apical dendrites of both layer 2a and layer 2b neurons, we observed the largest fractional increase in branch number in the first postnatal week (layer 2a: 75% of total increase in branchnumber, layer 2b: 90% of total increase in branch number, Fig. 2A2). For layer 2b neurons, we observed a significant increase in apical branch number between p0-2 and p6-8 (Fig. 2A2). Layer 2a neurons displayed a significant addition of proximal stems in the first postnatal week only (Fig. 2A4). Layer 2b neuron basal branches displayed a similar growth pattern (Fig. 3A2). Here, we observed a statistically significant increase in branch number in the first postnatal week (layer 2b: 64% of total increase in branch number, Fig. 3A2). In the shorter and less complex basal tree of layer 2a neurons (see above), significant branch addition was only evident when compared over the whole developmental period observed (Fig. 3A2).

After this initial determination of branch complexity by branch addition (growth phase 1), dendrites grew by branch elongation (growth phase 2). In layer 2a neurons, we observed statistically significant increases of the total apical dendritic branch length in the second postnatal week and between weeks 2 and 5 (Fig. 2A3). In layer 2b apical dendrites, the total dendritic branch length increased significantly in the first and second postnatal weeks (Fig. 2A3). In basal dendrites of layer 2b neurons, we observed increases in total dendritic branch length in growth phase two until p12-14 (Fig. 3A3). In the shorter and less complex basal tree of layer 2a neurons, significant length growth was again only evident when comparing over the whole developmental period observed (Fig. 3A3).

Increases in the total dendritic branch length are a combined effect of branch addition and elongation of individual branch segments. The dichotomy between branch addition in growth phase one and the length growth of existing branches in growth phase 2 became again apparent when examining the average branch length per neuron (Figs. 2B and 3B). In layer 2a and layer 2b neuron apical and basal branches, the average branch length per neuron did not increase in the first postnatal week. In the second postnatal week and between weeks 2 and 5, layer 2a and layer 2b neurons both displayed significant increases in the average apical branch length per neuron (Fig. 2B). A similar pattern was followed by layer 2b basal branches, the average branch length only increased significantly in the second postnatal week but not in the first postnatal week (Fig. 3B). In layer 2a neuron basal dendrites, length increase was only significant when comparing over the whole developmental period observed (Fig. 3A3). It is obvious from Fig. 3b that the relatively small length increase in layer 2a neuron basal dendrites predominantly occurred in the second postnatal week and between postnatal weeks 2 and 5. In sum, our measurements permitted us to clearly distinguish branch addition in growth phase one followed by elongation of individual branch segments in growth phase two for layer 2a and layer 2b dendrites.

We identified a third growth phase in the interval between the end of the second postnatal week (p12-14) and the fifth postnatal week (>p30). We observed a 34% reduction in the number of apical branches in layer 2b neurons and a 33% reduction in the number of stems in layer 2a neurons (Figs. 2A2 and 2A4). In layer 2b neurons, pruning was accompanied by a halt in the increase of total dendritic branch length (Fig. 2A3) despite a significant increase in the average branch length per neuron (Fig. 2B). This resulted in a diverging developmental trajectory of the apical dendrite between layer 2a and layer 2b neurons. While the total dendritic branch length was similar until week 2, the two different growth patterns of layer 2a and layer 2b neurons resulted in a significantly shorter apical dendritic tree in layer 2b neurons at five weeks (Fig. 2A3). Similar to their apical dendrites, layer 2b neuron basal dendrites pruned significantly after p12-14, both with respect to branch length and branch number (Fig. 3A2 and A3). Between postnatal weeks 2 and 5, we therefore defined a third growth phase of pruning for apical and basal dendrites of layer 2b neurons and apical stems of layer 2a neurons.

To see how the three distinct growth phases affected the spatial arrangement of branches, we plotted the distribution of branch densities as a function of distance from the soma. We observed differences between apical dendrites of layer 2a and layer 2b neurons during the first two postnatal weeks. In growth phase 1, layer 2a neurons branched close to the soma, the distribution was single-peaked (Fig. 2C1). In contrast, layer 2b neurons also displayed a second distal peak of branching right after birth (p1-2), and during the first growth phase determining dendritic complexity (p6-8; Fig. 2C2). During the second growth phase of dendritic elongation, no branches were added in layer 2a and layer 2b neurons. At the same time, we observed a right shift of the peaks of apical branch density to larger distances from the soma. This indicated that length growth was not limited to dendritic tips but also affected intermediate branches. Pruning in growth phase 3 resulted in a reduction of the second, distal peak of the layer 2b neurons, approximating the apical branch distributions of layer 2a and layer 2b neurons. The

distribution of basal branch density as a function of distance from the soma was similar for both cell types, with a right shift for layer 2b neurons (Fig. 3C).

In sum, compartment-specific differences in dendritic development were observed in growth phases one (branch addition) and three (pruning). While differences in basal branch number between layer 2a and layer 2b neurons were determined in growth phase one, development of the apical dendritic tree diverged during pruning in growth phase 3.

Figure 2

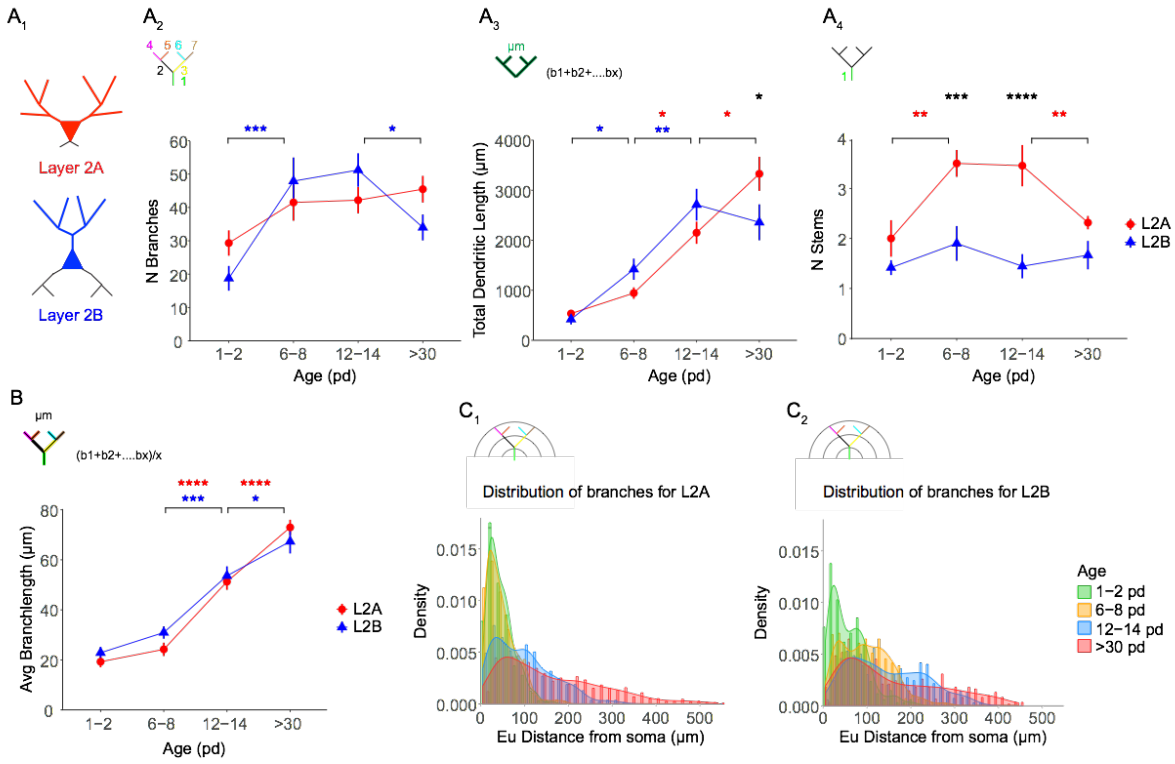

Figure 2

Developmental changes in the morphology of the apical dendritic trees

(A1) Visual representation of layer 2a (L2A, top, red) and layer 2b (L2B, bottom, blue) neurons. Morphological parameters were used to described growth patterns of the apical trees of these cells during development at four different ages (expressed as postnatal days, pd). Four measurements were extracted directly from the reconstructed cells: (A2) Total number of apical branches per cell (layer 2b neurons: p1-2 vs p6-8: $p < 0.001$, p12-14 vs >p30: $p<0.05$; ANOVA with Holm-Sidak's multiple comparisons test). (A3) total apical dendritic length per cell (layer 2a neurons: p6-8 vs p12-14: $p<0.05$, p12-14 vs >p30: $p<0.05$; layer 2b neurons: p1-2 vs p6-8: $p<0.05$, p6-8 vs p12-14: $p<0.01$; layer 2a vs layer 2b at >p30: $p<0.05$; ANOVA with Holm-Sidak's multiple comparisons test). (A4)

total number of apical stems per cell (layer 2a neurons: p1-2 vs p6-8: p< 0.01, p12-14 vs >p30: p<0.01; ANOVA with Holm-Sidak's multiple comparisons test). (B) Average apical branch-length per cell in µm (layer 2a neurons: p6-8 vs p12-14: p<0.0001, p12-14 vs >p30: p<0.0001; layer 2b neurons: p6-8 vs p12-14: p<0.001, p12-14 vs >p30: p<0.05; ANOVA with Holm-Sidak's multiple comparisons test). (C) Densities of the distributions of apical branches for layer 2a (C1) and layer 2b (C2) were plotted as function of the euclidean distance from the soma at four time windows: 1-2 pd (green), 6-8p pd (yellow), 12-14 pd (blue) and >30 pd (red). *: p<0.05, **: p<0.01, ***: p<0.001, ****: p<0.0001

Figure 3

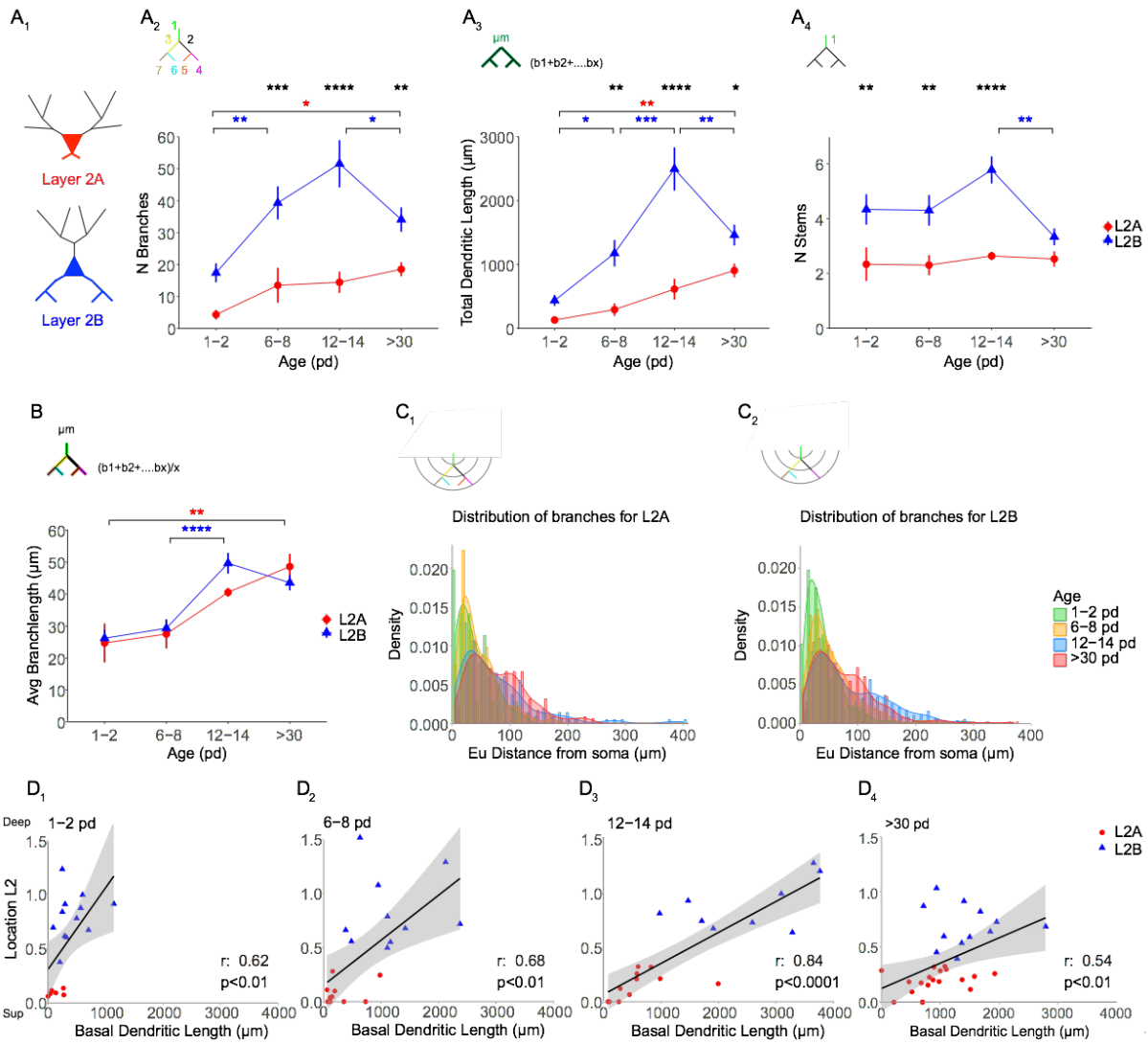

Figure 3

Developmental changes in the morphology of the basal dendritic tree

(A1) Visual representation of layer 2a (L2A, top, red) and layer 2b (L2B, bottom, blue) neurons. Morphological parameters were used to described growth patterns of the basal dendritic trees of layer 2a (L2A, red) and layer 2b

(L2B, blue) neurons during development at four different ages (expressed as postnatal days, pd). Four measurements were extracted directly from the reconstructed cells: (A2) Total number of basal branches per cell (layer 2a vs layer 2b: p6-8: $p<0.001$, p12-14: $p<0.0001$, >p30: $p<0.01$; layer 2b neurons: p1-2 vs p6-8: $p<0.01$, p12-14 vs >p30: $p<0.05$; layer 2a neurons: p1-2 vs p30: $p<0.05$; ANOVA with Holm-Sidak's multiple comparisons test) (A3) total basal dendritic length per cell in µm (layer 2a vs layer 2b: p6-8: $p<0.01$, p12-14: $p<0.0001$, >p30: $p<0.05$; layer 2b neurons: p0-2 vs p6-8: $p<0.05$, p6-8 vs p12-14: $p<0.001$, p12-14 vs >p30: $p<0.001$; layer 2a neurons: p1-2 vs >p30: $p<0.05$; ANOVA with Holm-Sidak's multiple comparisons test). (A4) total number of basal stems per cell and (B) average basal branch-length per cell in µm (layer 2b: p6-8 vs p12-14: $p<0.0001$; layer 2a: p1-2 vs >p30; ANOVA with Holm-Sidak's multiple comparisons test). (C) Densities of the distributions of basal branches for layer 2a (C1) and layer 2b (C2) were plotted as function of the euclidean distance from the soma at four time windows: p1-2 (green), p 6-8 (yellow), p 12-14 (blue) and >p30 (red). (D) total basal dendritic length versus the position of the cells in layer 2 at four time windows: p1-2 (D1, $r=0.62$, $p<0.01$), p6-8 (D2, $r=0.68$, $p<0.01$), p12-14 (D3, $r=0.84$, $p<0.0001$) and >p30 (D4, $r=0.54$, $p<0.01$); spearman correlation. *: $p<0.05$, **: $p<0.01$, ***: $p<0.001$, ****: $p<0.0001$

Ca^{2+} signaling patterns during early spontaneous network activity at the mesoscale population level

The complexity of both the apical and the basal dendritic tree is determined in the first postnatal week by branch addition (growth phase one). As dendritic structure and neuronal activity are interdependent, our next aim was to compare neuronal activity patterns during the first postnatal week between layer 2a and layer 2b neurons.

We first wanted to analyze differences between the two cell types at the mesoscale population level during immature slow spontaneous network activity patterns. Similarly to the somatosensory cortex, immature slow spontaneous network activity patterns in aPCx coexist with and can be triggered by sensory inputs starting at p0 (Hoffpauir et al. 2009; Leighton and Lohmann 2016). In acute brain slices, slow spontaneous network activity is preserved as a default state of the intrinsic recurrent network (Rigas et al. 2015). To date, these activity patterns have not been demonstrated in acute brain slices of the PCx. Here, we present evidence for the

occurrence of GDP-like events in the aPCx (Fig. 4). When looking at global events, activity was measured from a rectangular field of view covering layer 2 (Fig. 4A). For these measurements, we pooled population Ca^{2+} imaging in transgenic mice expressing GCaMP6f in excitatory neurons (Ai95-NexCre mice) and from acute brain slices bolus loaded with the synthetic Ca^{2+} indicator OGB1-AM. We observed a frequency of around 1 event/min during the first postnatal week. At the end of the second postnatal week, spontaneous activity in acute brain slices was virtually gone (Fig. 4B). GABAA-receptors have been proposed to be involved in the generation of GDPs (Ben-Ari et al. 2007; Allene et al. 2008). In acute brain slice preparations, activation of GABAA-receptors early in development is depolarizing and therefore a pharmacologiocal blockade of this type of receptors might result in a decrease of the frequency of the spontaneous events (Khazipov et al., 2015; but see Kirmse et al., 2015). In opposition, blockade of GABARs would in turn increase the frequency when GABA is hyperpolarizing. When plotting the net effect (Δ frequency) of the GABA antagonist Gabazine against postnatal days 1-13 there was a clear positive correlation from negative values (decrease in frequency) to positive values (increase in frequency; Fig. 4C). The time point at which the GABA antagonist Gabazine switches from reducing the frequency to increasing it was at p6 (Fig. 4C).

In the mature circuit, layer 2a neurons are less likely to be incorporated into recurrent circuits than layer 2b neurons (Suzuki and Bekkers 2011; Wiegand et al. 2011). To date, it is unclear whether immature spontaneous network activity reflects mature connectivity patterns or acts as an unstructured global signal. After having characterized spontaneous network activity in the aPCx, we therefore next wanted to test whether immature spontaneous network activity early in development differentially affects layer 2a and layer 2b neurons. Here, we only used data from Ai95-NexCre mice as this mouse line is specific for glutamatergic neurons. We plotted neuronal depth against the average percentage of coactive neurons as a measure of functional connectivity. Coactivity was significantly stronger in the deep layer 2b neurons (deep third of layer 2) than in superficial layer 2a neurons (superficial third of layer 2; Fig.4D). Already during

the first postnatal week, we observed higher functional connectivity and synchrony in layer 2b than in layer 2a neurons.

Figure 4

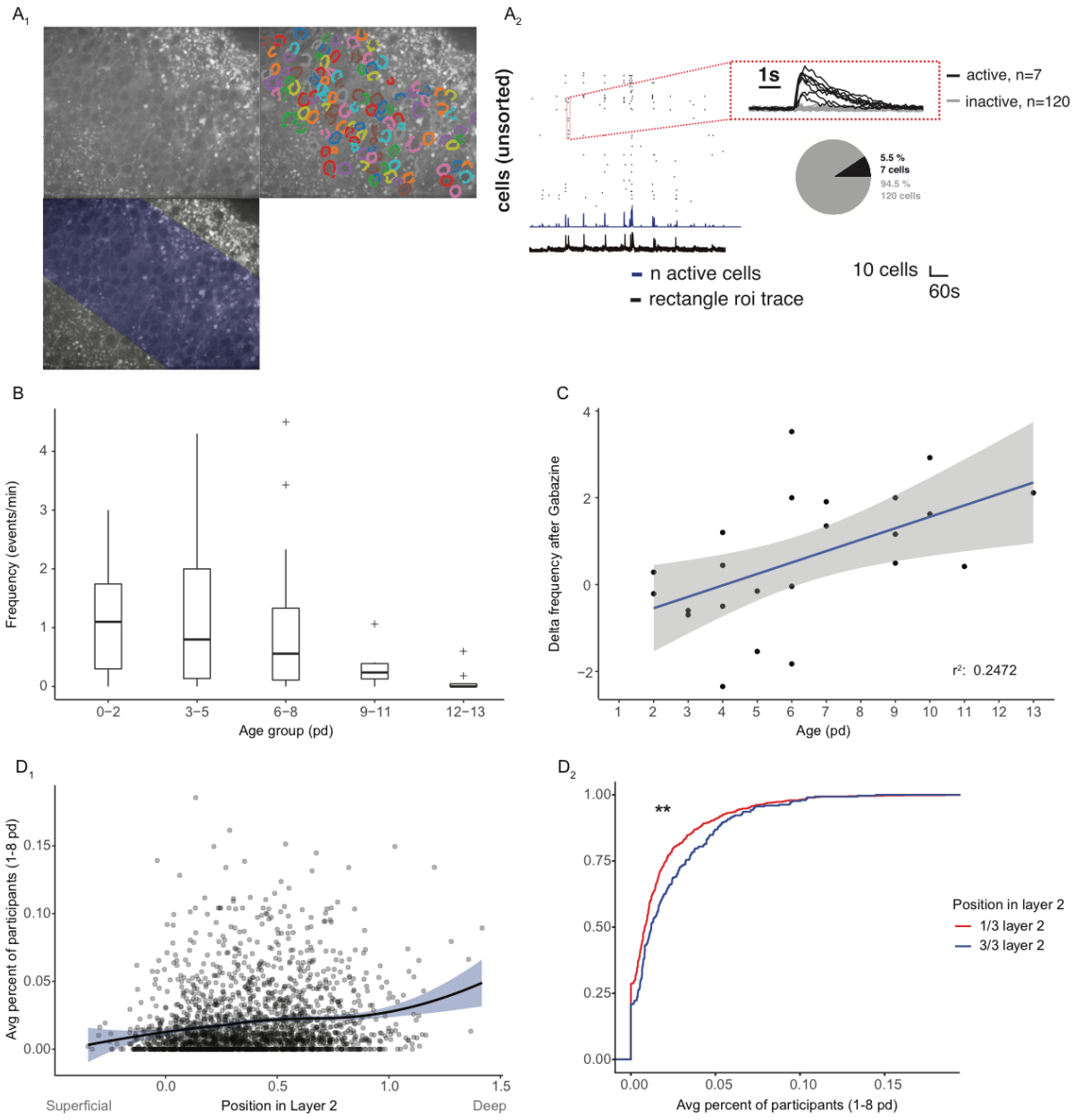

Figure 4

Comparison of spontaneous network activity in layer 2a and layer 2b neurons

(A1) Example of a baseline GCaMP-fluorescence image from an Ai95-NexCre mice. The field of view covers layer 2 in aPCx. Top Right: Detected cells in layer 2. Bottom: Rectangular ROI defined by the upper and lower boundaries of layer 2 for detecting global activity. (A2) Corresponding traces from the global events measured from the rectangular ROI (fluorescence: black trace, bottom) and the active cells (raster plot, blue trace for number of active cells, red inset for fluorescent traces from individual neurons in raster plot). The proportion of active versus

inactive cells is indicated by pie chart for one event. (B) Frequency of spontaneous events per minute measured at 5 different age groups (expressed as postnatal days, pd). (C) Scatter plot of delta frequency after gabazine (post-pre) against postnatal days 1 to 13 ($r=0.62$, $p<0.01$ measured with spearman correlation test). (D1) For each active neuron, the average percentage of coactive neurons accompanying spontaneous events was plotted against the position of the active neuron in layer 2 in the aPCx (data is fitted with a local polynomial regression and pooled from the first postnatal week). (D2) Layer 2 was divided in 3 parts. Cumulative distribution of the average percentage of coactive neurons from (D1) was plotted for the superficial third (red, 1/3 layer 2, corresponds to layer 2a neurons) and the deep third (blue, 3/3 layer 2, corresponds to layer 2b neurons; 1/3 layer 2 vs 3/3 layer 2: $p<0.01$; unpaired t-test). **: $p<0.01$.

Ca^{2+} signaling patterns during early spontaneous network activity at the dendritic level

Dendritic branch complexity is determined in the first postnatal week, during which we also observed spontaneous immature network activity. Our comparative analysis of population activity patterns at the mesoscale suggested that layer 2a and layer 2b neurons display different patterns of participation in these events. The main morphological difference between layer 2a and layer 2b neurons in postnatal week one was the lack of branch addition in the shorter and less complex basal tree of layer 2a neurons. We next wanted to analyze whether we could also observe subcellular differences in Ca^{2+} signaling related to this difference in dendritic growth between the two cell populations. We analyzed dendritic Ca^{2+} signals accompanying spontaneous network activity in individual neurons electroporated with the synthetic Ca^{2+} indicator OGB-1. To ensure that global Ca^{2+} signals observed at the single cell level were evoked by network activity, we recorded field EPSPs (fEPSPs) in parallel. We only analyzed dendritic activity accompanied by fEPSP signals indicative of spontaneous synchronized network activity (Fig. 5A2). Fast 3D time-lapse imaging permitted dendritic imaging on long dendritic segments. This way, it was possible to record global events on large stretches of first, second and third order dendrites. We divided the dendrites into 1.6 µm subsegments in which Ca^{2+} activity could be recorded individually (Fig. 5A1 and A3). As can be seen in Figs. 5A3 and

A4, activity was not evenly distributed over dendritic subsegments but displayed hotspots superimposed on global events. This result is qualitatively similar to an in vivo study analyzing sensory evoked global Ca^{2+} signals in the dendritic branches of OGB1-electroporated neurons in the developing tadpole tectum (Bollmann and Engert 2009). To further characterize these hotspots, we analyzed the Ca^{2+} traces of each individual 1.6 µm subsegment during single global dendritic events (see Fig. 5A4 for traces of each subsegment depicted in Fig. 5A1 during the one global event displayed in Fig. 5A2). Peaks of the individual subsegments were used to construct a profile of each global event.

Using this approach, we generated profiles of 45 global events from 11 apical branches on 8 layer 2a neurons and 44 global events from 17 apical branches on 4 layer 2b neurons. With respect to basal branches, we recorded profiles from 41 global events on 10 branches on 4 layer 2a neurons and 43 global events on 11 branches on 8 layer 2b neurons.

We performed Ca^{2+} imaging on electroporated neurons in order to minimize changes in intracellular fluid composition by whole cell patch clamp induced intracellular dialysis (Lang et al. 2006; Nevian and Helmchen 2007). Accordingly, it was not possible to relate dendritic Ca^{2+} signals to synaptic input strength, which most likely differed between spontaneous network events. In addition, local hotspots were superimposed on global events evoked by global depolarization from backpropagating APs. The number of APs during individual events could not be quantified either. Therefore, we implemented an analytical procedure to enhance inter-cell and inter-event comparability of individual hotspots (for details, see methods). The resulting median-corrected z-scores of the peaks of individual segment amplitudes were then compared for the different types of dendrites.

When we analyzed the median-corrected z-scores of the hotspots, they were comparable for apical dendrites on layer 2a and layer 2b neurons (Fig. 5B). The most striking growth difference in postnatal week one was the reduced branch addition in layer 2a basal dendrites (see above). This difference in structural growth was accompanied by significantly lower median-corrected

z-scores of Ca^{2+} hotspots in layer 2a neuron basal branches when compared to layer 2b hotspots (Fig. 5B).

We next analyzed the Ca^{2+} signals underlying hotspots pharmacologically. To generate reproducible and stable global signals, we applied extracellular electrical stimulation. Using this approach, we could generate global events with distinct Ca^{2+} hotspot profiles in apical dendrites of layer 2b neurons that were stable over the time course of a pharmacological experiment (Figs. 5C and F). We used peak $\Delta F/F$ values for comparing the hotspot amplitude before and after drug application. Under control conditions, peaks were unchanged after a 10 min waiting period and the peak difference (post-pre) was not significantly different from 0 (Figs. 5F and I). A major Ca^{2+} source in developing synapses is the NMDA-type glutamate receptor (NMDAR) (Leighton and Lohmann 2016). Indeed, blocking NMDARs with 50 µM of APV resulted in a significant reduction of the hotspot amplitudes (Figs. 5G and I). Recently, it was demonstrated in CA1 hippocampal neurons that NMDAR-mediated Ca^{2+} hotspots in developing dendrites were accompanied by a significant contribution of Ca^{2+} induced Ca^{2+} release (CICR) by Ryanodine Receptors (RyRs) after postnatal day 8 (Lee et al. 2016). In the aPCx, emptying of intracellular stores using CPA resulted in a small but significant decrease of the hotspot Ca2+ amplitude (Figs. 5 H and I).

These results substantiate the view that immature spontaneous network activity instructs structural growth by NMDAR and intracellular store mediated Ca^{2+} signals in a dose-dependent fashion (Wong and Ghosh 2002; Konur and Ghosh 2005; Lohmann 2009).

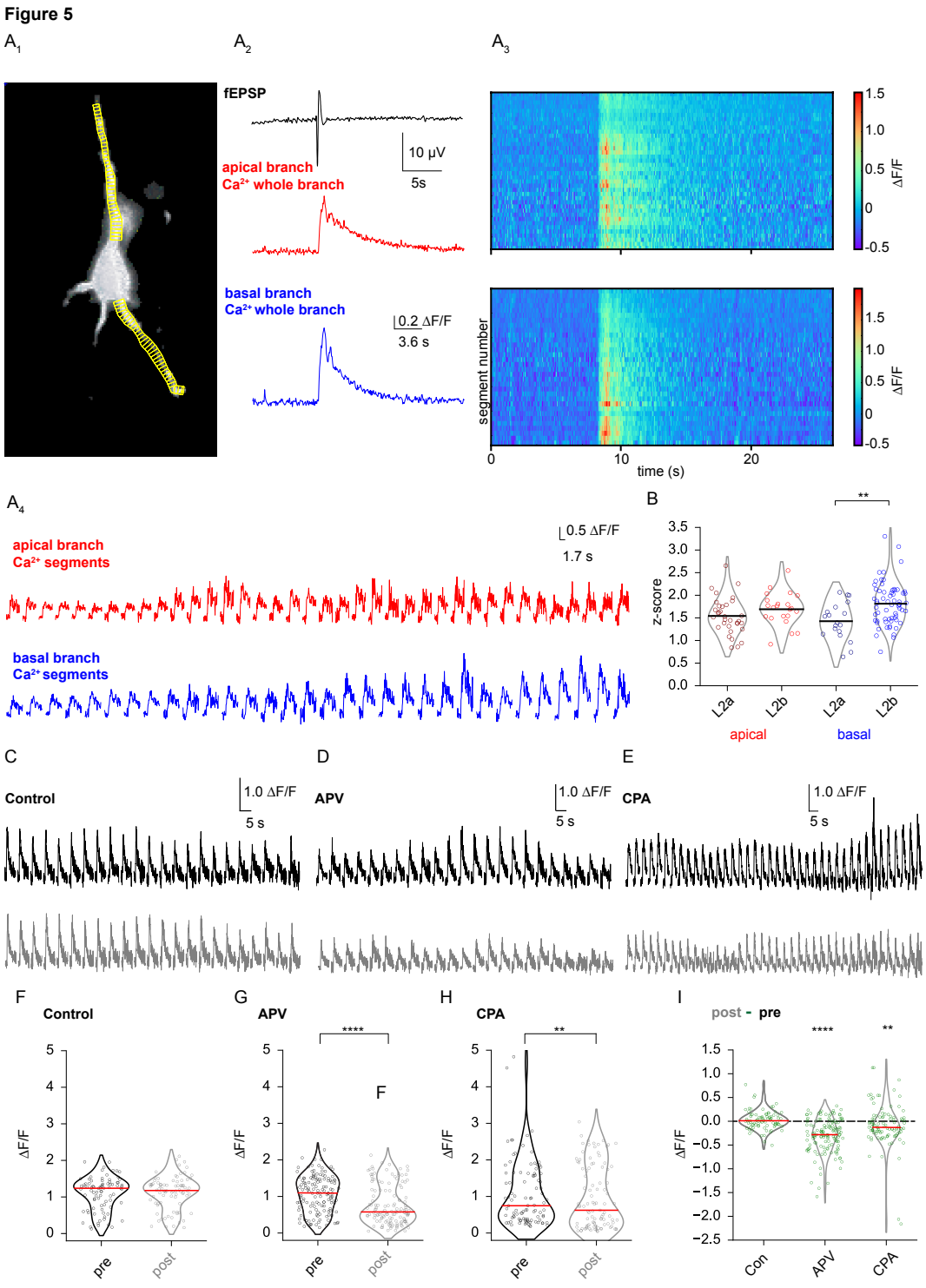

Figure 5

Ca²⁺ hotspots during spontaneous network activity

(A1) Overlay of the subsection of the electroporated neuron sampled for 3D timelapse imaging. Analyzed 1.6 µm segments are outlined by yellow boxes. (A2) Top: fEPSP indicating global spontaneous network activity. Middle: Corresponding fluorescence trace of the Ca^{2+} signal averaged over the whole apical branch imaged (blue). Bottom: Corresponding fluorescence trace of the Ca^{2+} signal averaged over the whole basal branch imaged (red). (A3) Top:

Spatial profile of Ca^{2+} response in the apical dendrite. Bottom: Spatial profile of Ca^{2+} response in the basal dendrite. (A4): Spatial profile of the single global spontaneous network event depicted in A(2) in apical (red) and basal dendrite (blue). Each trace corresponds to a yellow rectangular box in A(1) and to a horizontal pixel line in A(3). Peaks of the traces in (A4) constitute the dendritic profiles of individual global events. (B) Scatter plots on top of violin plots display median-corrected z-scores of the peaks in the branch profiles. Each point represents a spatially segregated hotspot. If the same hotspot was observed in several events, the z-score were averaged. Horizontal bars represent the mean z-scores. (apical dendrites: layer 2a (L2a): n=33; layer 2b (L2b): n=22; basal dendrites: L2a: n=19; L2b: n=64, L2a vs. L2b: $p<0.01$, ANOVA with Holm-Sidaks multiple comparisons test) (C-E) Top: Spatial profile of stimulus-evoked baseline Ca^{2+} response in the apical dendrite (black). Bottom: Spatial profile of stimulus-evoked Ca^{2+} response after 10 min (C: control interval, D: APV wash-in, E: CPA wash-in) in grey. (F) Scatter plots of averaged hotspot amplitudes before (pre) and after (post) 10 min control interval plotted on top of a violin plot, red line corresponds to median value (n=84/32/12 (hotspots/branches/neurons); n.s.; Wilcoxon matched pair test). (G) Scatter plots of averaged hotspot amplitudes before (pre) and after (post) 10 min of APV wash-in plotted on top of a violin plot, red line corresponds to median (n=136/52/11 (hotspots/branches/neurons); $p<0.0001$; Wilcoxon matched pair test). (H) Scatter plots of averaged hotspot amplitudes before (pre) and after (post) 10 min of CPA wash-in plotted on top of a violin plot, red line corresponds to median (n=99/43/15 (hotspots/branches/neurons); $p<0.01$, Wilcoxon matched pair test). (I) Scatter plots of the post-pre difference of averaged hotspot amplitudes from F-H on top of a violin plot, red line corresponds to median (APV: $p<0.0001$; CPA: $p<0.01$; Wilcoxon signed rank test against a theoretical difference of 0) **: $p<0.01$,****: $p<0.0001$

In the apical dendrite, pruning is limited to the sensory input layer 1a in layer 2b neurons

We described differences in Ca^{2+} signaling patterns correlated with differences in basal dendritic growth in the first postnatal week. Next, we wanted to further understand the developmental pattern of the apical dendritic tree. Here, the most pronounced differences occurred between the end of postnatal week two and the fifth postnatal week (growth phase 3). In this period, we observed selective pruning of layer 2b neuron apical dendrites, which did not occur in layer 2a neurons (see above).

The distinct organization of synaptic inputs to aPCx enabled us to relate pruning to specific circuits by grouping dendritic branches based on their position (layer 1a for branches receiving sensory inputs and layer 1b/2 for recurrent inputs). We therefore analyzed the growth and pruning patterns of apical dendrites with respect to the synaptic input layer the segments terminated in. Apical branches were categorized as branches terminating in layer 2, layer 1b (both recurrent) and 1a (sensory) for both cell types (Fig. 6A). Calretinin staining was used as a marker to delineate layer 1a (Fig. 1A4).

Proximal branches only receiving recurrent layer 1b and layer 2 input did not prune significantly in growth phase 3, both in layer 2a and in layer 2b neurons (Figs. 6B and C). Only in layer 2b neurons, distal branches that constituted sensory layer 1a circuits pruned significantly between p12-14 and >p30 (Fig. 6D). Here, pruning resulted both in a significant reduction of the number of layer 1a intermediate branches and tips (Figs. 6E1 and 2). Branch numbers in superficial layer 2a neurons remained stable over this developmental period (Figs. 6D and E). The reduction in branch number was accompanied by a significantly shorter layer 1a total dendritic length when comparing layer 2a and layer 2b neurons (Fig. 6F). Pruning was therefore limited to a specific circuit in a subpopulation of neurons.

To further understand circuit specific pruning of the apical dendrite, we compared the average branch length per neuron in layer 1a of layer 2a and layer 2b neurons between postnatal weeks two and five. We observed significant branch elongation of individual layer 1a branches for both cell types (Fig. 6G1). When comparing layer 2a and layer 2b neurons, the average branch length per neuron was similar after the second postnatal week. However, after the pruning phase, the average layer 1a branch length per neuron was significantly larger in layer 2b neurons (Fig. 6G1). When analyzing the distribution change of average branch lengths during the pruning phase, we saw a shift towards longer 1a branches in both cell types, with a more pronounced shift in 2b neurons (Figs. 6G2 and G3). In layer 2a neurons, we did not observe layer 1a branch loss. Here, the length increase could be explained by branch elongation, which

is a consequence of cortical growth. However, when interpreting the distribution shift in layer 2b neurons, we had to consider the pruning-related branch loss. The stronger right shift of the distribution towards longer branches in comparison to layer 2a neurons was accompanied by a significant decrease in branch number. This implied that pruning of sensory layer 1a branches in layer 2b neurons predominantly affected short branches or that surviving branches underwent enhanced length growth.

The preferential pruning of short branches is interesting in the light of recent findings regarding supralinear dendritic integration of sensory inputs in layer 1a branches of PCx layer 2b neurons. In aPCx layer 2b neurons, clustering of synaptic inputs on the same branch as opposed to distributed input to the entire dendritic arbor significantly modified the stimulus-response behavior. Clustered (same branch) input triggered NMDAR mediated Ca^{2+} spikes (NMDA-spikes) resulting in large local dendritic depolarization and associated Ca^{2+} influx. Distributed inputs of similar strength evoked substantially lower levels of dendritic depolarization (Kumar et al. 2018). Our experiments demonstrated that during postnatal development, pruning of the apical dendrites was mainly based on loss of short layer 1a branches (Fig. 6G). We hypothesized that the selection bias towards longer branch segments in the sensory synaptic input space of layer 2b neurons could be connected to supralinear dendritic integration in these neurons. This selection process would optimize the efficiency of the neuronal input-output function by promoting the growth and survival of branches receiving relevant clustered input.

Using modelling, we therefore wanted to test if the probability of supralinear integration by clustered inputs could indeed scale with branch length over our measured range of branch lengths. As a quantitative framework, we used the range of average branch lengths we observed at the beginning of the critical period (p12-14; 40 to 110 µm). The average total dendritic branch length (1800 µm) was constant for all neurons. We estimated the layer 1a input density based on a recent comprehensive quantitative description of mouse piriform cortex (Srinivasan and Stevens 2018). Based on Srinivasan and Stevens, we extrapolated that the whole population of

3700 bulbar glomeruli makes 2366 synapses with each individual neuron. 109 coincidently activated glomeruli would therefore activate 70 synapses on a layer 2b neuron, which we defined as the upper limit of coincident inputs. Fig. 6H2 displays the results of our calculation. We plotted the probability of dendritic NMDA-spikes evoked by clustering of more than 10 synapses on an individual branch as a function of the average branch length per neuron. This was repeated for different numbers of coincident synaptic inputs (see methods for details). As expected, the dendritic spike probability increased with increasing branch length. Within our parameter space, clustering probability and the resulting dendritic spiking increased up to 17% when comparing the shortest and longest average branch length we observed in our dataset. Quantitatively, our results suggest that, during our developmental time window, dendritic NMDA spikes are more likely to occur in long dendritic segments than short ones.

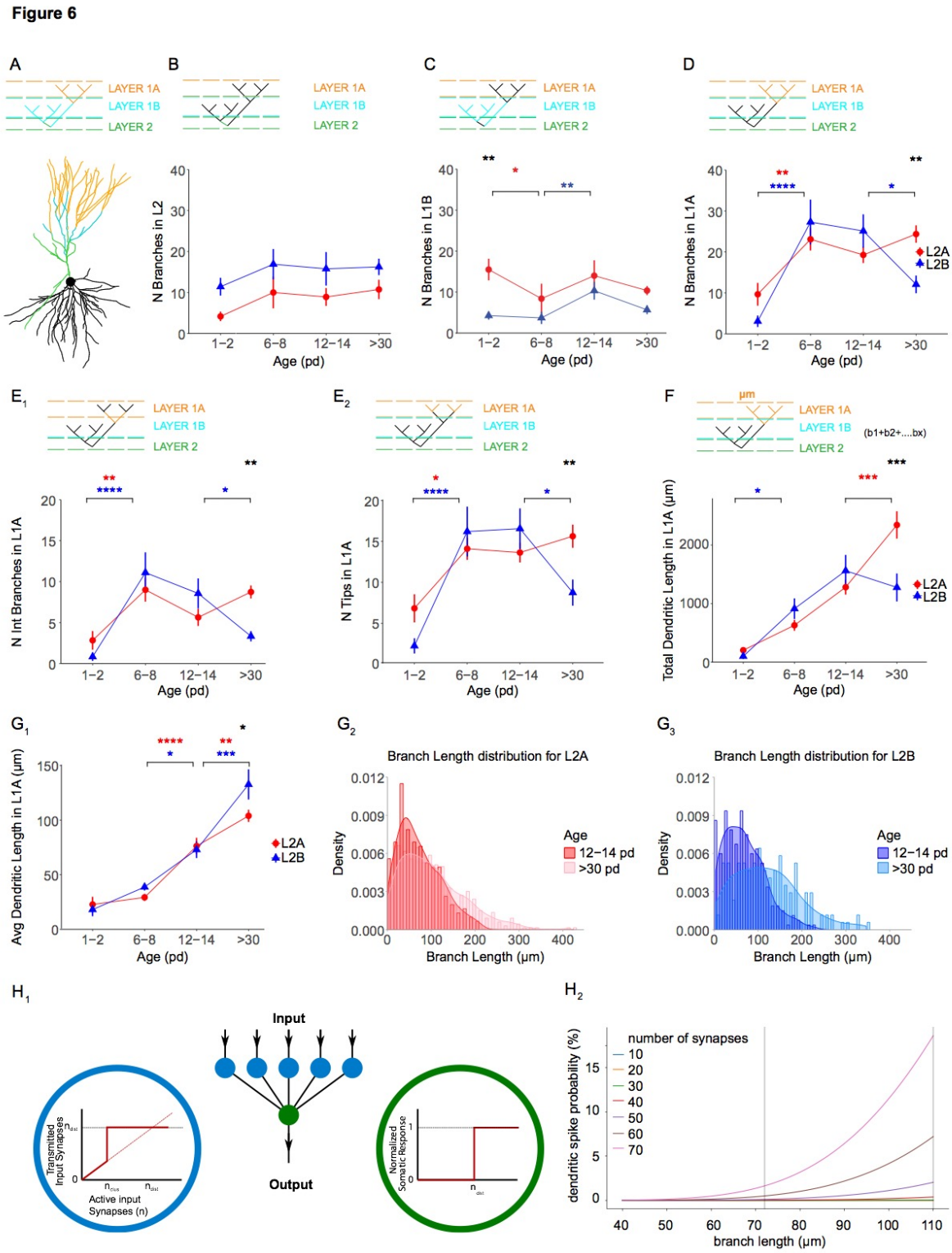

Figure 6

Differences in growth pattern of apical dendrites in response to layer specific synaptic inputs

(A) Example of a reconstructed cell shows the classification of the apical dendrites into three categories: branches terminating in layer 2 (L2, green), layer 1b (L1B cyan) and layer 1a (L1A, orange). (B-D) Comparison of the total

number of branches terminating in L2 (B), L1B (C, Kruskal-Wallis test with Dunn's multiple comparison) and L1A (D) for layer 2a (L2A, red) and layer 2b (L2B, blue) neurons (layer 2b neurons: p12-14 vs p30: $p<0.05$; ANOVA with Holm-Sidak's multiple comparisons test). (E-G) Growth patterns of the apical branches terminating in L1A including: Total number of intermediate branches per cell (E1, layer 2b neurons p12-p14 vs > p30: $p<0.05$, ANOVA with Holm-Sidak's multiple comparisons test), total number of tips per cell (E2, layer 2b neurons p12-p14 vs > p30: $p<0.05$, ANOVA with Holm-Sidak's multiple comparisons test), total dendritic length per cell (F, layer 2a vs layer 2b neurons at >p30: $p<0.001$, ANOVA with Holm-Sidak's multiple comparisons test), average branch length per cell (G1, p6-8 vs. p12-14: layer 2a neurons: $p<0.0001$, layer 2b neurons: $p<0.05$; p12-14 to <p30: layer 2a neurons: $p<0.01$ layer 2b neurons: $p<0.001$; layer 2a neurons vs layer 2b neurons at >p30: $p<0.05$; ANOVA with Holm-Sidak's multiple comparisons test) and densities of the distributions of the L1A branches for layer 2a (G2) and layer 2b (G3) plotted as function of branch length at two time windows: 12-14 pd (red and blue, respectively) and >30 pd (pink and light blue, respectively). (H1) Schematic neuron model as two-layered neural network, consisting of a dendritic activation layer (blue circles) and a somatic activation layer (green circles). The activation functions for the respective layers are shown in the insets. The activation of the soma is modeled as simple step function (if the input surpasses a certain threshold, the soma responds). The activation of every separate dendrite branch is modeled as an overlay of a linear response and a (non-linear) step function, to mimic the excitability of dendritic branches. If a dendritic branch is excited (due to a large enough number of same branch active input synapses) it transmits n_{dist}, triggering a somatic response. (H2) The response probability increases as function of the branch length, an effect that becomes more apparent for different increasing numbers of active input synapses S. *: $p<0.05$, **: $p<0.01$, ***: $p<0.001$, ****: $p<0.0001$

NMDA spikes are more pronounced in layer 1a dendrites of layer 2b neurons

So far, dendritic NMDA spikes have only been demonstrated in the anterior piriform cortex of rats older than four weeks (Kumar et al. 2018). Our calculations clearly demonstrated that they were more likely to occur in longer dendritic branches when performed on the branch lengths observed between p12 and p14. Here, we hypothesize that NMDA-spikes may play a role in the developmental branch selection observed in layer 1a dendrites of layer 2b neurons. To substantiate our hypothesis, we first wanted to test if layer 1a NMDA spikes also occur in layer 2b neurons during the second postnatal week. Layer 2a neurons did not show pruning but

equally distributed growth. If dendritic spiking enhanced selective pruning in distal apical dendrites of layer 2b neurons, another testable prediction would be an absence of dendritic spikes in layer 2a neurons.

We performed combined somatic whole cell patch clamp recordings and two-photon Ca^{2+} imaging in apical layer 1a branches of layer 2a and layer 2b neurons. Synaptic stimulation was achieved by focal electrical stimulation with theta-glass electrodes (Figs. 7 A4 and B4). Using Ca^{2+} imaging, we first identified a focal stimulation spot. Stimulation strength was then linearly increased. When plotting the area under the curve (AUC) of the EPSP in layer 2b neurons, we observed a distinct nonlinear increase at specific stimulation strengths, which was abolished after washing in of the NMDAR-antagonist APV (Fig. 7A3). In addition, this increase displayed the typical shape of an NMDA-spike (Fig. 7A1). We performed Ca^{2+} imaging in parallel and could further observe that the nonlinear enhancement of the EPSP AUC was accompanied by a branch-specific increase in spatial spread and amplitude of the Ca^{2+} transient (Fig. 7A5). These hallmarks of nonlinear dendritic NMDA spikes were not observed in layer 2a neurons (Fig. 7B). Next, we plotted the AUC and the amplitude of layer 2a and layer 2b neuron EPSPs before and after wash-in of APV. We observed a significant decrease of both parameters in layer 2b neurons. In contrast, NMDAR-block by APV did not affect AUCs and amplitudes of EPSPs in layer 2a neurons (Figs 7 C1and C2). At the stimulation site, the stimulation-evoked Ca^{2+} signal of both layer 2a and layer 2b neurons was significantly reduced by APV (Fig. 7D). Under NMDAR-block by APV, the AUC and the amplitude of the EPSP constitute a readout of the AMPA-type glutamate receptor mediated depolarization. Consequently, the absolute value of the AUC and the amplitude in APV reflected the synaptic input strength of our stimulation. These values were not significantly different between layer 2a and layer 2b neurons in our sample, indicating comparable stimulation strength for both cell types (Fig. 7C).

We conclude that, in contrast to layer 2b neurons, layer 2a neurons do not display layer 1a NMDA-spikes at comparable input strengths. These spikes can be observed during the

developmental period of dendritic pruning of short dendritic segments in layer 2b neurons. In layer 2a neurons, we neither observe pruning nor NMDA spikes in the same developmental period.

Figure 7

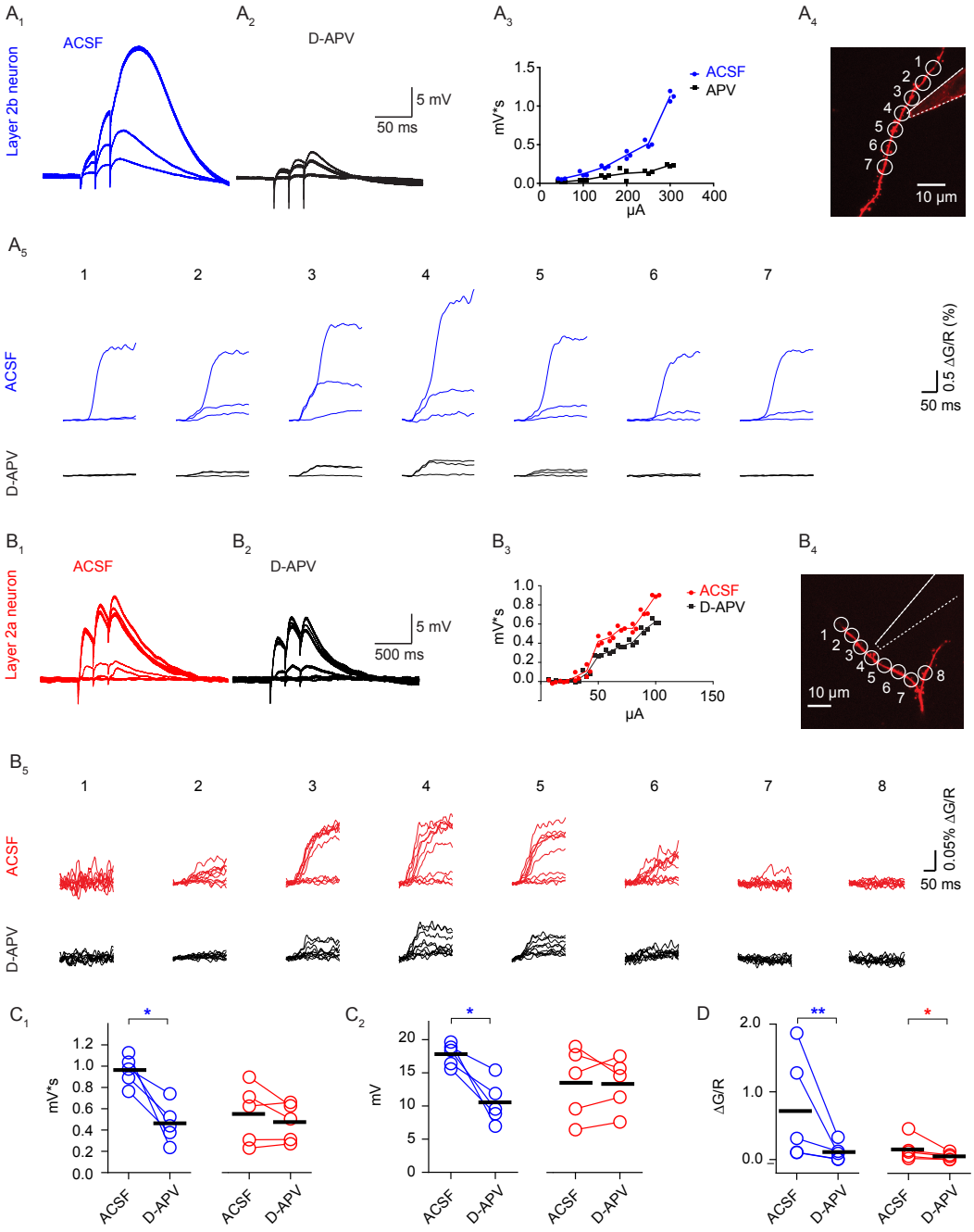

Figure 7

Dendritic NMDA-spikes can only be observed in layer 2b neurons

(A) displays a representative layer 2b neuron, (B) a representative layer 2a neuron. (A1/B1) Overlay of electric responses measured at the soma upon electrical stimulation with linear strength increase in layer 1a. (A2/B2)

Response to same stimulus after application of APV. (A3/B3) Plot of stimulation strength against area under the curve from the same cell. (A4/B4) Imaged dendritic branch and position of the stimulation electrode. (A5/B5) Fluorescence traces of Ca^{2+} responses at ROIs outlined in A4/B4 under baseline conditions (upper rows, blue and red) and after application of APV (lower rows, black). Increasing stimulation strengths are overlayed. (C1) Area under the curve (AUC) before and after application of APV in layer 2b neurons (blue) and layer 2a neurons (red; layer 2b, pre vs. post: $p<0.05$; layer 2a, pre vs. post: $p=0.18$, paired t test; layer 2a post vs. layer 2b post : $p=0.92$, t-test). (C2) EPSP amplitude before and after application of APV in layer 2b neurons (blue) and layer 2a neurons (red; layer 2a, pre vs. post: $p<0.05$; layer 2b, pre vs. post: $p=0.7$; paired t test; layer 2a post vs. layer 2b post: $p=0.25$, t-test). (D) Fluorescent Ca^{2+} response before and after application of APV in layer 2b neurons (blue) and layer 2a neurons (red; layer 2b, pre vs. post: $p<0.01$, paired t test; layer 2a, pre vs. post: $p<0.05$, paired t test). *: $p<0.05$, **: $p<0.01$.

Functional consequences of differences in nonlinear integration of sensory inputs between layer 2a and layer 2b neurons

What are the functional consequences of the exclusive presence of layer 1a NMDA-spikes in layer 2b neurons? In addition to the proposed role in dendritic development, they may also have an impact on olfactory sensory processing. Recently, a clear functional segregation of neurons in the aPCx with respect to the responsiveness to variations in odor concentrations has been described (Roland et al. 2017). From the single neuron perspective, the main discriminative feature for odor intensity was the onset latency of the response in the aPCx. On the population level, this resulted in differences in synchrony affecting the peak mean population response. It was possible to distinguish two populations of neurons. A subpopulation of concentration-invariant neurons displayed uniform short onset latencies independent of odorant concentration. The subpopulation of concentration-variant neurons showed longer latencies at low odorant concentrations that systematically decreased at higher odorant concentrations (Bolding et al., 2017). To date, it is unclear what distinguishes these two neuronal populations.

Differences in dendritic integration could serve as a biophysical mechanism underlying the functional segregation in these two groups. Nonlinear integration of sensory inputs in layer 2b neurons resulting in all-or none regenerative dendritic spikes could result in invariant short-latency onsets. In contrast, the linear integration mode of sensory inputs in layer 2a neurons would be a cellular mechanism compatible with concentration-variant latencies.

We applied modeling to test this hypothesis. To study the effect of non-linear dendritic integration, we compared the stimulus response relationship of a linear integrate-and-fire-or burst (IFB) neuron (Casti et al. 2002; Smith et al. 2000) with a non-linear IFB neuron. The non-linear dendritic integration behavior of non-linear IFB neurons is captured by incorporating a membrane potential-dependent conductance for the synaptic current. Odor intensity is relayed by shifts of response latencies in the olfactory bulb population output (Stern et al. 2018). We know there is a fixed time interval in which aPCx principal neurons are responsive to excitatory bulb input before inhibition dominates. If one further assumes that odorants activate several distinct glomeruli, the consequence of a shift in response latency would be that the aPCx target neuron of a group of olfactory glomeruli would receive more bulbar mitral cell inputs in a shorter time frame. We therefore displayed changes in odorant concentrations as changes in bulbar input rate. Results of this simulation study are shown in Figure 8. Fig. 8A illustrates the deterministic case. In Fig. 8A1, membrane potential changes for linear IFB and non-linear IFB neurons are displayed for a regular input spike train with constant interspike intervals. In this example we observed that non-linear dendritic integration (based for example upon NMDA-spikes) could decrease the response latency significantly. We next analyzed the onset latency as a function of input frequency. For increasing input rates, the response latency decreased for both linear IFB and non-linear IFB neurons (Fig. 8A2). This effect was also evident in the corresponding raster plots where the spike times were displayed for a range of input rates (Figs. 8A3 and 4). When comparing the latency over the same range of input frequencies, linear IFB neurons covered a large range of latencies from long to short. In comparison, non-linear IFB

neurons had a narrower range of shorter latencies as described for concentration-invariant neurons (Fig 8A).

To test how dendritic properties shape the response of neuronal populations, we illustrated response characteristics to noisy input (Fig. 8B). We investigated the response to poisson-distributed input spike trains with fixed mean rates. Fig. 8B1 depicts a voltage trace for a noisy input spike train in a linear IFB with mean rate E=100 Hz. Population responses consisted of the averaged response of a model neuron to a set of different noisy input spike trains. Raster plots in Figs. 8B2 and B4 depict responses for linear IFB and non-linear IFB model neurons, respectively, for a mean input rate of 100 and 150 Hz. Figs. 8B3 and B5 show the corresponding mean population response rates. Input-frequency dependent changes of the dynamics of the mean population response rate differed between the linear IFB and non-linear IFB model neurons. Non-linear IFB neuron onset latency, synchrony and maximal mean population response rate displayed relatively minor changes (Fig. 8B5). These changes were more pronounced in linear IFB neurons (Fig. 8B3). The observed differences corresponded to the biphasic population responses indicative of concentration variant and invariant neurons demonstrated in Bolding et al. (Bolding et al. 2017). We conclude that differences in dendritic integration between layer 2a and layer 2b neurons could position layer 2a neurons as concentration variant neurons and layer 2b neurons as concentration invariant neurons.

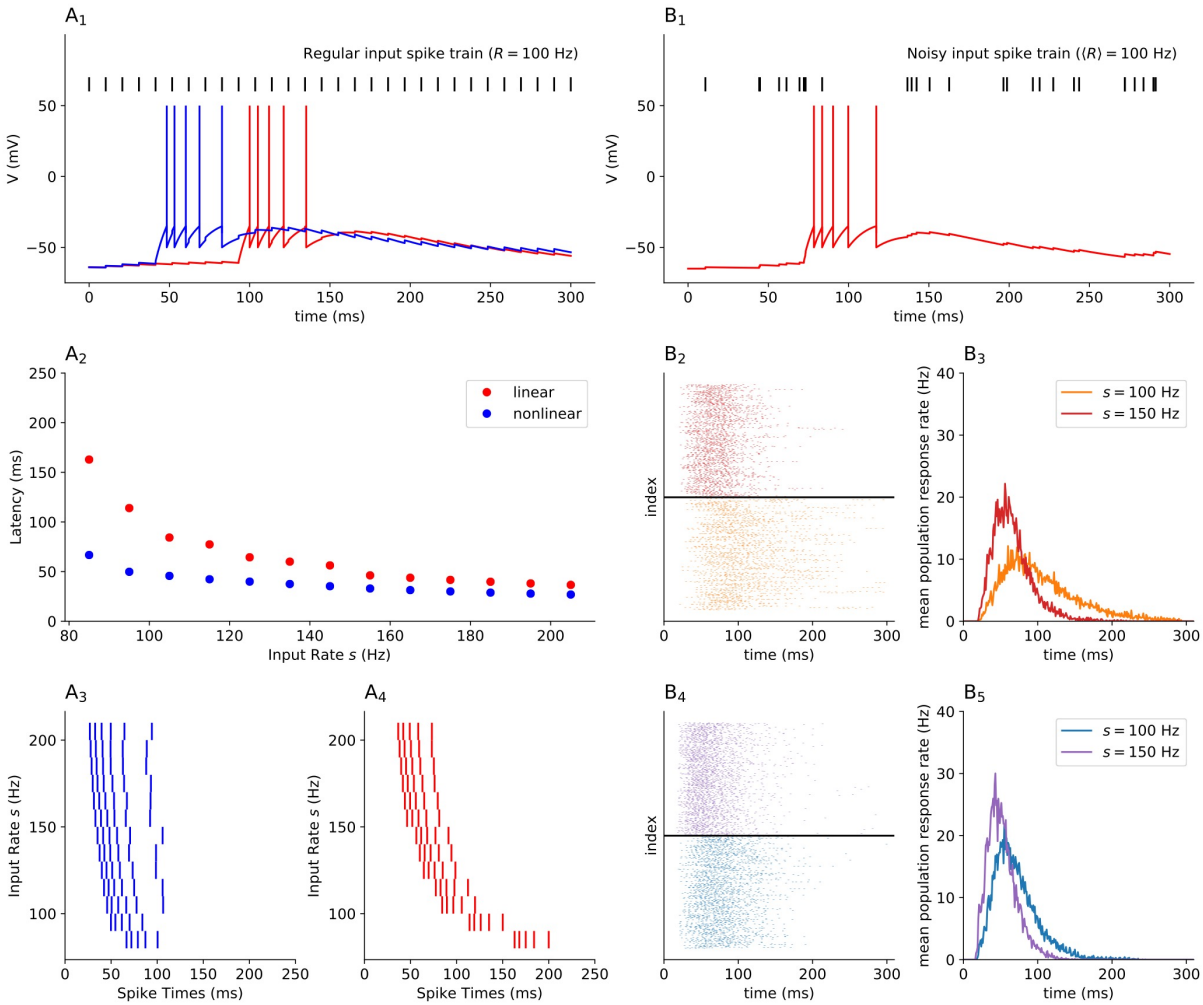

Figure 8: Nonlinear dendritic integration of glomerular inputs co-determines the onset latency of cortical responses

(A) Comparison of the characteristics of the non-linear (blue lines and symbols) and linear (red lines and symbols) model neuron for the deterministic (noise-less) case. (A1) Voltage traces of a linear (red) and a non-linear (blue) model neuron in response to a regular input spike train with rate R=100 Hz. Vertical black lines show the input spike train. (A2) Response latency for the linear (red) and non-linear (blue) model neuron as function of the input spike rate. For smaller input rates, the latency of the linear model neuron is significantly larger than for the non-linear model neuron. (A3, A4): Raster plots, showing the spike times as function of the input rate for the linear (red and non-linear (blue) model neuron.

Illustrations in B show a comparison of the non-linear and linear model neuron in case in response to noisy input spike trains (Poisson events). (B1) Exemplary voltage trace of a linear model neuron in response to a noisy input spike train with mean rate $\langle R \rangle$=100 Hz. Vertical lines show the input spike train. (B2, B4) Raster plot, showing exemplary response spikes of the linear model neuron (B2) and the non-linear model neuron (B4) in response to noisy input spike trains with mean rate $\langle R \rangle$=100 Hz (orange, blue) and $\langle R \rangle$=150 Hz (red, purple). (B3, B5) Mean

population response rate over time in colors corresponding to the results shown in B2 and B4.

Discussion

Here, we performed a morphometric and functional analysis of postnatal dendritic development in aPCx sensory and recurrent circuits. We compared developmental patterns in layer 2a neurons and layer 2b neurons, two neighboring cell types in layer 2 with distinct sensory and recurrent wiring. We distinguished three growth phases: 1. Branch addition (growth phase one, postnatal week one). 2. Branch elongation (growth phase two, postnatal week two) 3. Branch pruning (growth phase 3, postnatal weeks 3-5). We discovered circuit and cell-type specific differences in dendritic development in growth phases one and three. In growth phase one, layer 2a neuron basal dendrites incorporated in recurrent circuits branched significantly less than layer 2b neuron basal dendrites. This was accompanied by less synchronous participation in spontaneous network activity of layer 2a neurons. In addition, spontaneous network activity evoked local Ca^{2+} signals were reduced in layer 2a neuron basal dendrites. In growth phase three, pruning of apical dendrites receiving layer 1a sensory inputs was only observed in layer 2b neurons, but not in layer 2a neurons. Pruning was clearly biased towards shorter dendritic branches. Using electrophysiology, Ca^{2+} imaging and modeling, we demonstrated how NMDA-spike mediated nonlinear amplification of inputs could support the survival and growth of long dendritic branches. We propose that dendritic Ca^{2+} influx via NMDARs dose-dependently directs dendritic growth in growth phases one and three. We further related the observation that NMDA-spikes are more likely to occur in layer 2b neurons to olfactory information processing. To this end, we present a model demonstrating that concentration invariant odor coding is facilitated by nonlinear integration of clustered dendritic input in layer 2b neurons. This sheds new light on how the 'multiplexed representation of odor concentration and identity' (Stern et al. 2018) in aPCx can be explained by cell-type specific differences in dendritic integration.

Ca^{2+} serves as a compartment-specific dendritotrophic signal during neuronal development

Dendritic growth is a complex biological phenomenon utilizing a plethora of signaling mechanisms (Ledda and Paratcha 2017; Menon and Gupton 2018; Jan and Jan 2010). Within this complex signaling network, Ca^{2+} signals play a central role when it comes to linking neuronal activity to dendritic growth (Wong and Ghosh 2002; Konur and Ghosh 2005; Lohmann 2009). Subcellular differences in the amplitude profile of global Ca^{2+} signals evoked by immature spontaneous network activity in the first postnatal week (growth phase one) are of special interest. In this time period, immature spontaneous network activity overlaps with substantial dendritic growth in the majority of brain regions (Konur and Ghosh 2005). To the best of our knowledge, in mammals, spontaneous immature network activity evoked dendritic Ca^{2+} signals have not been characterized so far with respect to their impact on dendritic development.

Comparing layer 2a and layer 2b neurons, we have two adjacent cell types sharing similar (apical dendrite) and dissimilar (basal dendrite) developmental trajectories of their dendritic tree during the first postnatal week. Comparing the same dendritic compartments on different cell types provides insights on how the profile of dendritic Ca^{2+} signaling amplitudes during immature spontaneous activity relates to dendritic growth. Apical dendrites displayed similar dendritic Ca^{2+} signals in both cell types. In contrast, the stunted basal dendrites of layer 2a neurons displayed comparatively smaller amplitude Ca^{2+} signals than layer 2b neurons, which developed an elaborate basal dendritic tree. It has been shown previously that synaptically activated NMDARs induce enhanced morphological plasticity and dendritic growth in developing hippocampal neurons in slice culture (Wayman et al. 2006; Maletic-Savatic et al. 1999). In tadpoles, visual activity induced dendritic growth requires NMDAR activation (Sin et al. 2002). In chick retina ganglion cells, local Ca^{2+} transients promote dendritic growth

(Lohmann et al. 2002). Our findings are in line with a straightforward concept of a dose-dependent promotion of dendritic growth and branching by large compartmentalized NMDAR-mediated Ca^{2+} signals enhanced by Ca^{2+} release from intracellular stores during immature spontaneous network activity. We extend previous findings from non-mammalian preparations and artificial stimulation in slice cultures to spontaneously occurring naturalistic stimulus patterns in mammalian acute brain slices. It is interesting to speculate whether the higher synchrony in layer 2b neurons underlies the comparatively larger compartmentalized Ca^{2+} signals in their basal dendrites.

In growth phase three, we also observed differences in the growth patterns of layer 2a and layer 2b neurons that were accompanied by different Ca^{2+} signaling mechanisms. Dendritic NMDA-spikes are accompanied by large localized Ca^{2+} transients (Kumar et al. 2018), which are generally considered growth-promoting (Konur and Ghosh 2005). Between p14 and p21, NMDA-spikes were observed in layer 1a dendrites of layer 2b neurons, which showed pruning in that period. Layer 2a neurons did not prune 1a branches nor did they display dendritic NMDA-spikes. This may indicate that NMDAR-spike mediated Ca^{2+} signaling has an impact on dendritic development. We observed the majority of apical dendritic branch loss in short layer 1a dendrites of layer 2b neurons. At the same time, our calculations demonstrated that the probability of NMDA-spikes is lower in short dendritic segments. Therefore, one could expect more frequent occurrence of NMDA-spikes in longer apical dendritic branches of layer 2b neurons during the pruning period. Accordingly, longer segments would display optimized input-output functions resulting in larger NMDA-spike mediated dendritotrophic Ca^{2+} signals. This could promote the survival and elongation of long branches at the expense of short branches. The result would be the structural self-amplification of dendritic NMDA-spikes by promoting branches with a higher probability for clustered inputs. Interestingly, the time window of this process matched the critical period of NMDAR-dependent circuit specific sensory synaptic plasticity in layer 1a (Franks and Isaacson 2005) (Poo and Isaacson 2011). We

therefore propose that in layer 2b neurons, the critical period in the aPCx is accompanied by circuit specific pruning and remodeling of the distal apical dendritic tree receiving sensory inputs in layer 1a.

In sum, dose-dependent Ca^{2+} signaling mechanisms observed at distinct developmental stages in different subcircuits support the hypothesis that Ca^{2+} serves as a compartment-specific dendritotrophic signal during neuronal development. However, it will require longitudinal in vivo studies to directly demonstrate that Ca^{2+} signals dose-dependently regulate dendritic growth during developmental patterning in growth phases one and three.

Differences in development between the topographic neocortex and the non-topographic aPCx

The aPCx is a sensory brain region with a simple and evolutionary conserved structure that predates the development of the sensory neocortex (Bekkers and Suzuki 2013). When thinking about the dendritic architecture, a central difference between sensory neocortex and the aPCx is the spatial organization of afferent input. Sensory neocortex is a topographic circuit: nearby peripheral neurons share similar and predictable representations of sensory space and contact neighboring cortical neurons. These sensory-input sharing neighboring neurons have a high degree of local connectivity. In contrast, the PCx is a distributed, non-topographic circuit, where both the representation of sensory space and the recurrent connectivity are unpredictable and dispersed (Srinivasan and Stevens 2018). This diffuse organization of the palaeocortical PCx is likely to reflect the primordial structure of sensory cortices prior to the evolution of isocortex in synapsids and later mammals (Fournier et al. 2015). In the following, we would like to compare our data with published neocortical patterns of dendritic growth.

The determination of branch complexity during the first postnatal week corresponds to dendritic growth patterns identified in layer 2/3 and layer V pyramidal neurons in rodent neocortex (Petit et al. 1988; Maravall et al. 2004; Romand et al. 2011). As in our dataset, length

increase of neocortical dendrites was significant between the first and second postnatal week both in basal and apical dendrites. In these studies, there was no further increase in the period until p30 (Petit et al. 1988; Romand et al. 2011). Growth phase three observed here is where the developmental trajectories of neocortex and palaeocortex diverge: In the palaeocortical aPCx, we observed a reduction in length growth and a significant reduction in dendritic branch number in apical and basal dendrites beween p12-14 and p30. In neocortical layer 5 neurons, a decrease in branch number most likely due to pruning of filopodia was observed earlier, between p7 and p14 in apical but not in basal dendrites (Romand et al. 2011).

We propose that an overabundance of dendrites during the critical period is a consequence of the requirements of a non-topographic afferent input structure. Overabundance of dendrites increases the combinatorial space for different glomerular input combinations and for recurrent connections between neurons sharing these connections. The related increase in the possibility of glomerular input combinations on distinct branches maybe necessary in a distributed circuit like the PCx. In contrast, the topographic neocortex displays local clustering of similar featured inputs. This will result in a higher probability of the clustering of similar inputs on locally interconnected neurons. An effect of topographical organisation may therefore be the effective wiring of significant features of sensory space. This would obviate the need for the metabolically expensive generation of superfluous dendritic branches during development.

In the aPCx, the overabundance of dendrites combined with pruning could therefore enhance the initial combinatorial space and compensate for the lack of effective wiring by topography biases. Our data suggests an NMDA-spike dependent selection and optimization process. This would greatly enhance the computational power of a non-topographic system. We hypothesize that NMDA-spikes would enhance the survival and optimize the input-output function of dendritic branches coding for relevant features in interconnected neurons sharing sensory and recurrent inputs.

Functional implications of differences between layer 2a and layer 2b neuron dendrites

In layer 2, we can distinguish at least two different types of principle cells based on their position, connectivity and morphology (Suzuki and Bekkers 2011; Wiegand et al. 2011). Layer 2a neurons and layer 2b neurons have been hypothesized to represent two parallel streams of olfactory information processing. However, this dichotomy is complicated by the observation that morphologically, there seems to be a continuum between so called semilunar cells with no basal dendrites and superficial pyramidal cells with elaborate basal dendrites (Bekkers and Suzuki 2013). Our detailed morphological reconstructions and analysis support the idea of a continuum between neurons with short or absent basal dendrites in layer 2a and neurons with more elaborate basal dendrites in layer 2b. A previously unnoticed difference between layer 2a and layer 2b neurons is the larger dendritic tree of layer 2a neurons in the sensory layer 1a. This fits well with the stronger incorporation into sensory circuits these neurons display, and may have implications for the size of their olfactory receptive fields.

Recent studies have extended the parameter space for splitting aPCx layer 2 neurons: long-range tracing studies identified layer-specific differences in axonal projection patterns (Chen et al. 2014; Diodato et al. 2016; Mazo et al. 2017). Different excitatory cell types have also been identified at the level of genetic markers (Diodato et al. 2016). These findings further support the notion of more than 2 subclasses of neurons in aPCx layer 2. This is reflected by a range of putative functionally different cell populations. An example of a cortical functional segregation in the aPCx not inherited from the olfactory bulb is the distinction between concentration variant and identity coding/concentration invariant neurons (Roland et al. 2017; Bolding et al. 2017).

To date, it is unclear how the abovementioned functional difference between concentration variant and identity coding/concentration invariant neurons is generated by the PCx. We observed that sensory inputs can drive supralinear dendritic NMDA-spikes only in layer 2b

neurons. Our experimental findings and modeling results suggest that this difference between layer 2a and layer 2b neurons could be a cellular mechanism that determines whether a neuron falls into the concentration variant or the identity coding/concentration invariant category. In concentration variant neurons, different odorant concentrations are translated into differences in the onset latency of the spiking response. In contrast, identity coding/concentration invariant neurons display uniform short onset latencies of the spiking response. This early onset population also contains the relevant information on odor identity (Roland et al. 2017; Bolding et al. 2017; Stern et al. 2018). When considering our model, the larger range of onset delays in nonlinearly integrating layer 2a neurons suggests that they could constitute the population of concentration variant neurons. Neurons in this functional subclass change their response latency as a function of odor concentration. Our model further demonstrated that sensory responses evoking nonlinear dendritic NMDA-spikes could result in uniformly distributed short onsets in layer 2b neurons. This mechanism makes layer 2b neurons good candidates for the concentration invariant subpopulation of neurons defining odor identity. Dendritic spiking of sensory inputs is facilitated by recurrent inputs in the aPCx (Kumar et al. 2018). This amplification mechanism is ideally suited to rapidly activate interconnected ensembles of aPCx layer 2b neurons identifying an odor.

In addition, dendritic NMDA-spikes evoked by coincident sensory and recurrent inputs have implications for memory-related pattern completion in the aPCx: synaptic plasticity in the aPCx depends on spine Ca^{2+} signal amplitude (Johenning et al. 2009). Dendritic spiking evoked by coincident sensory and recurrent inputs would generate large local Ca^{2+} transients in the activated dendritic branches. This nonlinear integration of sensory and recurrent inputs could serve as a plasticity inducing coincidence detection mechanism. Such a mechanism would amplify synaptic connections between ensembles of recurrently connected neurons that share similar sensory inputs. We hypothesize that this could be a key mechanism underlying pattern completion from degraded inputs that has been recently identified as an exclusive property of

layer 2b neurons (Bolding et al. 2019). In sum, we demonstrated that different developmental trajectories of the dendritic tree in layer 2a and layer 2b neurons are associated with differences in dendritic integration. These differences can be linked to specific functions. Our data therefore support the concept that structural and functional differences between layer 2a and layer 2b neuron dendritic trees determine their distinct functions in the aPCx.

Funding

This work was supported by the Deutsche Forschungsgemeinschaft (German Research Foundation)
(SFB 1315 Project-ID 327654276 to D.S., Exc 2049 to D.S., SPP 1665 to D.S., JO 1079/3-1 to F.J., RU1660/5-1 to S.R.), Bundesministerium für Bildung und Forschung (Federal Ministry of Education and Research)(01GQ1420B to D.S.), ERC BrainPlay-Synergy grant (D.S.)

Acknowledgements

We would like to thank Robert Sachdev and Matthew Larkum for the Ai95 mouse line. We would further like to thank Anke Schönherr and Susanne Rieckmann for excellent technical assistance.

References

Allene C, Cattani A, Ackman JB, Bonifazi P, Aniksztejn L, Ben-Ari Y, Cossart R. 2008. Sequential Generation of Two Distinct Synapse-Driven Network Patterns in Developing Neocortex. J Neurosci. 28:12851–12863.

Bekkers JM, Suzuki N. 2013. Neurons and circuits for odor processing in the piriform cortex. Trends Neurosci. 36:429–438.

Ben-Ari Y, Gaiarsa JL, Tyzio R, Khazipov R. 2007. GABA: A Pioneer Transmitter That Excites Immature Neurons and Generates Primitive Oscillations. Physiological Reviews. 87:1215–1284.

Bolding KA, Franks KM. 2017. Complementary codes for odor identity and intensity in olfactory cortex. Elife. 6.

Bolding KA, Nagappan S, Han B, Wang F, Franks KM. 2019. Pattern recovery by recurrent circuits in piriform cortex. bioRxiv. 51:418–458.

Bollmann JH, Engert F. 2009. Subcellular Topography of Visually Driven Dendritic Activity in the Vertebrate Visual System. Neuron. 61:895–905.

Casti A, Omurtag A, Sornborger A, Kaplan E, Knight B, Victor J, Sirovich L. 2002. A population study of integrate-and-fire-or-burst neurons. Neural Comput. 14:957–986.

Chen C-FF, Zou D-J, Altomare CG, Xu L, Greer CA, Firestein SJ. 2014. Nonsensory target-dependent organization of piriform cortex. Proceedings of the National Academy of Sciences. 111:16931–16936.

Choy JMC, Suzuki N, Shima Y, Budisantoso T, Nelson SB, Bekkers JM. 2017. Optogenetic Mapping of Intracortical Circuits Originating from Semilunar Cells in the Piriform Cortex. Cereb Cortex. 27:589–601.

Demir R, Haberly LB, Jackson MB. 2001. Epileptiform discharges with in-vivo-like features in slices of rat piriform cortex with longitudinal association fibers. Journal of Neurophysiology. 86:2445–2460.

Diodato A, de Brimont MR, Yim YS, Derian N, Perrin S, Pouch J, Klatzmann D, Garel S, Choi GB, Fleischmann A. 2016. Molecular signatures of neural connectivity in the olfactory cortex. Nat Commun. 7:1–10.

Feng L, Zhao T, Kim J. 2015. Neutube 1.0: A new design for efficient neuron reconstruction software based on the swc format. eNeuro.

Fournier J, Müller CM, Laurent G. 2015. ScienceDirectLooking for the roots of cortical sensory computation in three-layered cortices. Current Opinion in Neurobiology. 31:119–126.

Franks KM, Isaacson JS. 2005. Synapse-specific downregulation of NMDA receptors by early experience: a critical period for plasticity of sensory input to olfactory cortex. Neuron. 47:101–114.

Goebbels S, Bormuth I, Bode U, Hermanson O, Schwab MH, Nave K-A. 2006. Genetic targeting of principal neurons in neocortex and hippocampus of NEX-Cre mice. genesis. 44:611–621.

Hanganu-Opatz IL. 2010. Between molecules and experience: Role of early patterns of coordinated activity for the development of cortical maps and sensory abilities. Brain Research Reviews. 64:160–176.

Hoffpauir BK, Marrs GS, Mathers PH, Spirou GA. 2009. A comparison of three sensory systems in mice. Brain Research. 1277:115–129.

Jan YN, Jan LY. 2010. Branching out: Mechanisms of dendritic arborization. Nat Rev Neurosci. 11:316–328.

Johenning FW, Beed PS, Trimbuch T, Bendels MHK, Winterer J, Schmitz D. 2009. Dendritic compartment and neuronal output mode determine pathway-specific long-term potentiation in the piriform cortex. J Neurosci. 29:13649–13661.

Johenning FW, Theis A-K, Pannasch U, Rückl M, Rüdiger S, Schmitz D. 2015. Ryanodine

Receptor Activation Induces Long-Term Plasticity of Spine Calcium Dynamics. PLoS Biol. 13:e1002181.

Kaczorowski CC, Disterhoft J, Spruston N. 2007. Stability and plasticity of intrinsic membrane properties in hippocampal CA1 pyramidal neurons: effects of internal anions. The Journal of Physiology. 578:799–818.

Kanari L, Ramaswamy S, Shi Y, Morand S, Meystre J, Perin R, Abdellah M, Wang Y, Hess K, Markram H. 2019. Objective Morphological Classification of Neocortical Pyramidal Cells. Cerebral Cortex. 29:1719–1735.

Khazipov R, Luhmann HJ. 2006. Early patterns of electrical activity in the developing cerebral cortex of humans and rodents. Trends in Neurosciences. 29:414–418.

Khazipov R, Valeeva G, Khalilov I. 2015. Depolarizing GABA and developmental epilepsies. CNS Neurosci Ther. 21:83–91.

Kirmse K, Kummer M, Kovalchuk Y, Witte OW, Garaschuk O, Holthoff K. 2015. GABA depolarizes immature neurons and inhibits network activity in the neonatal neocortex in vivo. Nat Commun. 6:1–13.

Konur S, Ghosh A. 2005. Calcium Signaling and the Control of Dendritic Development. Neuron. 46:401–405.

Kumar A, Schiff O, Barkai E, Mel BW, Poleg-Polsky A, Schiller J. 2018. NMDA spikes mediate amplification of inputs in the rat piriform cortex. Elife. 7.

Lang SB, Bonhoeffer T, Lohmann C. 2006. Simultaneous imaging of morphological plasticity and calcium dynamics in dendrites. Nat Protoc. 1:1859–1864.

Lanoue V, Cooper HM. 2018. Branching mechanisms shaping dendrite architecture. Developmental Biology. 451:1–9.

Ledda F, Paratcha G. 2017. Mechanisms regulating dendritic arbor patterning. Cell Mol Life Sci. 74:4511–4537.

Lee KFH, Soares C, Thivierge JP, Béïque JC. 2016. Correlated Synaptic Inputs Drive Dendritic Calcium Amplification and Cooperative Plasticity during Clustered Synapse Development. Neuron. 89:784–799.

Leighton AH, Lohmann C. 2016. The Wiring of Developing Sensory Circuits—From Patterned Spontaneous Activity to Synaptic Plasticity Mechanisms. Front Neural Circuits. 10:219.

Lohmann C. 2009. Calcium signaling and the development of specific neuronal connections. Prog Brain Res. 175:443–452.

Lohmann C, Myhr KL, Wong ROL. 2002. Transmitter-evoked local calcium release stabilizes developing dendrites. Nature. 418:177–181.

Madisen L, Garner AR, Shimaoka D, Chuong AS, Klapoetke NC, Li L, van der Bourg A, Niino Y, Egolf L, Monetti C, Gu H, Mills M, Cheng A, Tasic B, Nguyen TN, Sunkin SM, Benucci A, Nagy A, Miyawaki A, Helmchen F, Empson RM, Knöpfel T, Boyden ES, Reid RC, Carandini M, Zeng H. 2015. Transgenic Mice for Intersectional Targeting of Neural Sensors and Effectors with High Specificity and Performance. Neuron. 85:942–958.

Maletic-Savatic M, Malinow R, Svoboda K. 1999. Rapid dendritic morphogenesis in CA1 hippocampal dendrites induced by synaptic activity. Science (80-). 283:1923–1927.

Maravall M. 2004. Experience-dependent Changes in Basal Dendritic Branching of Layer 2/3 Pyramidal Neurons During a Critical Period for Developmental Plasticity in Rat Barrel Cortex. Cerebral Cortex. 14:655–664.

Martin-Lopez E, Ishiguro K, Greer CA. 2017. The Laminar Organization of Piriform Cortex Follows a Selective Developmental and Migratory Program Established by Cell Lineage. Cerebral Cortex. 29:1–16.

Mazo C, Grimaud J, Shima Y, Murthy VN, Lau CG. 2017. Distinct projection patterns of different classes of layer 2 principal neurons in the olfactory cortex. Scientific Reports. 7:1–10.

Menon S, Gupton S. 2018. Recent advances in branching mechanisms underlying neuronal morphogenesis. F1000Res. 7:1779–12.
Nevian T, Helmchen F. 2007. Calcium indicator loading of neurons using single-cell electroporation. Pflugers Arch. 454:675–688.
Pachitariu M, Stringer C, Schröder S, Dipoppa M, Rossi LF, Carandini M, Harris KD. 2016. Suite2p: beyond 10,000 neurons with standard two-photon microscopy, bioRxiv.
Petit TL, LeBoutillier JC, Gregorio A, Libstug H. 1988. The pattern of dendritic development in the cerebral cortex of the rat. Brain Research. 469:209–219.
Poirazi P, Brannon T, Mel BW. 2003. Pyramidal neuron as two-layer neural network. Neuron. 37:989–999.
Poo C, Isaacson JS. 2007. An Early Critical Period for Long-Term Plasticity and Structural Modification of Sensory Synapses in Olfactory Cortex. J Neurosci. 27:7553–7558.
Poo C, Isaacson JS. 2011. A Major Role for Intracortical Circuits in the Strength and Tuning of Odor-Evoked Excitation in Olfactory Cortex. Neuron. 72:41–48.
Rigas P, Adamos DA, Sigalas C, Tsakanikas P, Laskaris NA, Skaliora I. 2015. Spontaneous Up states in vitro: a single-metric index of the functional maturation and regional differentiation of the cerebral cortex. Front Neural Circuits. 9:219.
Roland B, Deneux T, Franks KM, Bathellier B, Fleischmann A. 2017. Odor identity coding by distributed ensembles of neurons in the mouse olfactory cortex. eLife. 6:14255.
Romand S, Wang Y, Toledo-Rodriguez M, Markram H. 2011. Morphological Development of Thick-Tufted Layer V Pyramidal Cells in the Rat Somatosensory Cortex. Front Neuroanat. 5:1–27.
Rueckl M, Lenzi SC, Moreno-Velasquez L, Parthier D, Schmitz D, Ruediger S, Johenning FW. 2017. SamuROI, a Python-Based Software Tool for Visualization and Analysis of Dynamic Time Series Imaging at Multiple Spatial Scales. Front Neuroinform. 11:1059–14.
Sarma AA, Richard MB, Greer CA. 2011. Developmental Dynamics of Piriform Cortex. Cerebral Cortex. 21:1231–1245.
Scorcioni R, Polavaram S, Ascoli GA. 2008. L-Measure: a web-accessible tool for the analysis, comparison and search of digital reconstructions of neuronal morphologies. Nat Protoc. 3:866–876.
Sin WC, Haas K, Ruthazer ES, Cline HT. 2002. Dendrite growth increased by visual activity requires NMDA receptor and Rho GTPases. Nature. 419:475–480.
Smith GD, Cox CL, Sherman SM, Rinzel J. 2000. Fourier analysis of sinusoidally driven thalamocortical relay neurons and a minimal integrate-and-fire-or-burst model. J Neurophysiol. 83:588–610.
Sommer C, Straehle C, Kothe U, Hamprecht FA. 2011. Ilastik: Interactive learning and segmentation toolkit. Proc - Int Symp Biomed Imaging. 230–233.
Srinivasan S, Stevens CF. 2018. The distributed circuit within the piriform cortex makes odor discrimination robust. J Comp Neurol. 1–44.
Stern M, Bolding KA, Abbott LF, Franks KM. 2018. A transformation from temporal to ensemble coding in a model of piriform cortex. Elife. 7:865.
Suzuki N, Bekkers JM. 2006. Neural coding by two classes of principal cells in the mouse piriform cortex. J Neurosci. 26:11938–11947.
Suzuki N, Bekkers JM. 2010. Inhibitory neurons in the anterior piriform cortex of the mouse: classification using molecular markers. J Comp Neurol. 518:1670–1687.
Suzuki N, Bekkers JM. 2011. Two layers of synaptic processing by principal neurons in piriform cortex. J Neurosci. 31:2156–2166.
Torben-Nielsen B. 2014. An Efficient and Extendable Python Library to Analyze Neuronal Morphologies. Neuroinform. 12:619–622.
Wayman GA, Impey S, Marks D, Saneyoshi T, Grant WF, Derkach V, Soderling TR. 2006. Activity-Dependent Dendritic Arborization Mediated by CaM-Kinase I Activation and

Enhanced CREB-Dependent Transcription of Wnt-2. Neuron. 50:897–909.
Wiegand HF, Beed P, Bendels MHK, Leibold C, Schmitz D, Johenning FW. 2011. Complementary Sensory and Associative Microcircuitry in Primary Olfactory Cortex. J Neurosci. 31:12149–12158.
Wilson DA, Sullivan RM. 2011. Cortical Processing of Odor Objects. Neuron. 72:506–519.
Wong ROL, Ghosh A. 2002. Activity-dependent regulation of dendritic growth and patterning. Nat Rev Neurosci. 3:803–812.

Figure legends

Figure 1

Localization and differentiation of the two principle neurons in Layer 2 of the aPCx

(A) Slice containing one recorded neuron filled with biocytin (A1) and additionally, post hoc labelled with DAPI (A2) and calretinin (A3). The overlay (A4) shows the recorded neuron located in Layer 2b of the aPCx. (B) 3D Morphological reconstructions of different layer 2a (B1) and layer 2b (B2) neurons at four time windows: Right after birth (p1-2), at the end of the first postnatal week (p6-8), at the end of the second postnatal week (p12-14) and after the fifth postnatal week (>p30). Soma and apical dendrites are in black and basal dendrites in red. Scalebar 100 µm.

Figure 2

Developmental changes in the morphology of the apical dendritic trees

(A1) Visual representation of layer 2a (L2A, top, red) and layer 2b (L2B, bottom, blue) neurons. Morphological parameters were used to described growth patterns of the apical trees of these cells during development at four different ages (expressed as postnatal days, pd). Four measurements were extracted directly from the reconstructed cells: (A2) Total number of apical

branches per cell (layer 2b neurons: p1-2 vs p6-8: p< 0.001, p12-14 vs >p30: p<0.05; ANOVA with Holm-Sidak's multiple comparisons test). (A3) total apical dendritic length per cell (layer 2a neurons: p6-8 vs p12-14: p<0.05, p12-14 vs >p30: p<0.05; layer 2b neurons: p1-2 vs p6-8: p<0.05, p6-8 vs p12-14: p<0.01; layer 2a vs layer 2b at >p30: p<0.05; ANOVA with Holm-Sidak's multiple comparisons test). (A4) total number of apical stems per cell (layer 2a neurons: p1-2 vs p6-8: p< 0.01, p12-14 vs >p30: p<0.01; ANOVA with Holm-Sidak's multiple comparisons test). (B) Average apical branch-length per cell in µm (layer 2a neurons: p6-8 vs p12-14: p<0.0001, p12-14 vs >p30: p<0.0001; layer 2b neurons: p6-8 vs p12-14: p<0.001, p12-14 vs >p30: p<0.05; ANOVA with Holm-Sidak's multiple comparisons test). (C) Densities of the distributions of apical branches for layer 2a (C1) and layer 2b (C2) were plotted as function of the euclidean distance from the soma at four time windows: 1-2 pd (green), 6-8p pd (yellow), 12-14 pd (blue) and >30 pd (red). *: p<0.05, **: p<0.01, ***: p<0.001, ****: p<0.0001

Figure 3

Developmental changes in the morphology of the basal dendritic tree

(A1) Visual representation of layer 2a (L2A, top, red) and layer 2b (L2B, bottom, blue) neurons. Morphological parameters were used to described growth patterns of the basal dendritic trees of layer 2a (L2A, red) and layer 2b (L2B, blue) neurons during development at four different ages (expressed as postnatal days, pd). Four measurements were extracted directly from the reconstructed cells: (A2) Total number of basal branches per cell (layer 2a vs layer 2b: p6-8: p<0.001, p12-14: p<0.0001, >p30: p<0.01; layer 2b neurons: p1-2 vs p6-8: p<0.01, p12-14 vs >p30: p< 0.05; layer 2a neurons: p1-2 vs p30: p<0.05; ANOVA with Holm-Sidak's multiple comparisons test) (A3) total basal dendritic length per cell in µm (layer 2a vs layer 2b: p6-8: p<0.01, p12-14: p<0.0001, >p30: p<0.05; layer 2b neurons: p0-2 vs p6-8: p<0.05, p6-8 vs p12-14: p<0.001, p12-14 vs >p30: p<0.001; layer 2a neurons: p1-2 vs >p30: p<0.05; ANOVA with Holm-Sidak's multiple comparisons test). (A4) total number of basal stems per cell and (B)

average basal branch-length per cell in µm (layer 2b: p6-8 vs p12-14: $p<0.0001$; layer 2a: p1-2 vs >p30; ANOVA with Holm-Sidak's multiple comparisons test). (C) Densities of the distributions of basal branches for layer 2a (C1) and layer 2b (C2) were plotted as function of the euclidean distance from the soma at four time windows: p1-2 (green), p 6-8 (yellow), p 12-14 (blue) and >p30 (red). (D) total basal dendritic length versus the position of the cells in layer 2 at four time windows: p1-2 (D1, $r=0.62$, $p<0.01$), p6-8 (D2, $r=0.68$, $p<0.01$), p12-14 (D3, $r=0.84$, $p<0.0001$) and >p30 (D4, $r=0.54$, $p<0.01$); spearman correlation. *: $p<0.05$, **: $p<0.01$, ***: $p<0.001$, ****: $p<0.0001$

Figure 4

Comparison of spontaneous network activity in layer 2a and layer 2b neurons

(A1) Example of a baseline GCaMP-fluorescence image from an Ai95-NexCre mice. The field of view covers layer 2 in aPCx. Top Right: Detected cells in layer 2. Bottom: Rectangular ROI defined by the upper and lower boundaries of layer 2 for detecting global activity. (A2) Corresponding traces from the global events measured from the rectangular ROI (fluorescence: black trace, bottom) and the active cells (raster plot, blue trace for number of active cells, red inset for fluorescent traces from individual neurons in raster plot). The proportion of active versus inactive cells is indicated by pie chart for one event. (B) Frequency of spontaneous events per minute measured at 5 different age groups (expressed as postnatal days, pd). (C) Scatter plot of delta frequency after gabazine (post-pre) against postnatal days 1 to 13 ($r=0.62$, $p<0.01$ measured with spearman correlation test). (D1) For each active neuron, the average percentage of coactive neurons accompanying spontaneous events was plotted against the position of the active neuron in layer 2 in the aPCx (data is fitted with a local polynomial regression and pooled from the first postnatal week). (D2) Layer 2 was divided in 3 parts. Cumulative distribution of the average percentage of coactive neurons from (D1) was plotted for the superficial third (red,

1/3 layer 2, corresponds to layer 2a neurons) and the deep third (blue, 3/3 layer 2, corresponds to layer 2b neurons; 1/3 layer 2 vs 3/3 layer 2: $p<0.01$; unpaired t-test). **: $p<0.01$.

Figure 5

Ca^{2+} hotspots during spontaneous network activity

(A1) Overlay of the subsection of the electroporated neuron sampled for 3D timelapse imaging. Analyzed 1.6 µm segments are outlined by yellow boxes. (A2) Top: fEPSP indicating global spontaneous network activity. Middle: Corresponding fluorescence trace of the Ca^{2+} signal averaged over the whole apical branch imaged (blue). Bottom: Corresponding fluorescence trace of the Ca^{2+} signal averaged over the whole basal branch imaged (red). (A3) Top: Spatial profile of Ca^{2+} response in the apical dendrite. Bottom: Spatial profile of Ca^{2+} response in the basal dendrite. (A4): Spatial profile of the single global spontaneous network event depicted in A(2) in apical (red) and basal dendrite (blue). Each trace corresponds to a yellow rectangular box in A(1) and to a horizontal pixel line in A(3). Peaks of the traces in (A4) constitute the dendritic profiles of individual global events. (B) Scatter plots on top of violin plots display median-corrected z-scores of the peaks in the branch profiles. Each point represents a spatially segregated hotspot. If the same hotspot was observed in several events, the z-score were averaged. Horizontal bars represent the mean z-scores. (apical dendrites: layer 2a (L2a): n=33; layer 2b (L2b): n=22; basal dendrites: L2a: n=19; L2b: n=64, L2a vs. L2b: $p<0.01$, ANOVA with Holm-Sidaks multiple comparisons test) (C-E) Top: Spatial profile of stimulus-evoked baseline Ca^{2+} response in the apical dendrite (black). Bottom: Spatial profile of stimulus-evoked Ca^{2+} response after 10 min (C: control interval, D: APV wash-in, E: CPA wash-in) in grey. (F) Scatter plots of averaged hotspot amplitudes before (pre) and after (post) 10 min control interval plotted on top of a violin plot, red line corresponds to median value (n=84/32/12 (hotspots/branches/neurons); n.s.; Wilcoxon matched pair test). (G) Scatter plots of averaged hotspot amplitudes before (pre) and after (post) 10 min of APV wash-in plotted on top of a violin

plot, red line corresponds to median (n=136/52/11 (hotspots/branches/neurons); p<0.0001; Wilcoxon matched pair test). (H) Scatter plots of averaged hotspot amplitudes before (pre) and after (post) 10 min of CPA wash-in plotted on top of a violin plot, red line corresponds to median (n=99/43/15 (hotspots/branches/neurons); p<0.01, Wilcoxon matched pair test). (I) Scatter plots of the post-pre difference of averaged hotspot amplitudes from F-H on top of a violin plot, red line corresponds to median (APV: p<0.0001; CPA: p<0.01; Wilcoxon signed rank test against a theoretical difference of 0) **: p<0.01 ,****: p<0.0001

Figure 6

Differences in growth pattern of apical dendrites in response to layer specific synaptic inputs

(A) Example of a reconstructed cell shows the classification of the apical dendrites into three categories: branches terminating in layer 2 (L2, green), layer 1b (L1B cyan) and layer 1a (L1A, orange). (B-D) Comparison of the total number of branches terminating in L2 (B), L1B (C, Kruskal-Wallis test with Dunn's multiple comparison) and L1A (D) for layer 2a (L2A, red) and layer 2b (L2B, blue) neurons (layer 2b neurons: p12-14 vs p30: p<0.05; ANOVA with Holm-Sidak's multiple comparisons test). (E-G) Growth patterns of the apical branches terminating in L1A including: Total number of intermediate branches per cell (E1, layer 2b neurons p12-p14 vs > p30: p<0.05, ANOVA with Holm-Sidak's multiple comparisons test), total number of tips per cell (E2, layer 2b neurons p12-p14 vs > p30: p<0.05, ANOVA with Holm-Sidak's multiple comparisons test), total dendritic length per cell (F, layer 2a vs layer 2b neurons at >p30: p<0.001, ANOVA with Holm-Sidak's multiple comparisons test), average branch length per cell (G1, p6-8 vs. p12-14: layer 2a neurons: p<0.0001, layer 2b neurons: p<0.05; p12-14 to <p30: layer 2a neurons: p<0.01 layer 2b neurons: p<0.001; layer 2a neurons vs layer 2b neurons at >p30: p<0.05; ANOVA with Holm-Sidak's multiple comparisons test) and densities

of the distributions of the L1A branches for layer 2a (G2) and layer 2b (G3) plotted as function of branch length at two time windows: 12-14 pd (red and blue, respectively) and >30 pd (pink and light blue, respectively). (H1) Schematic neuron model as two-layered neural network, consisting of a dendritic activation layer (blue circles) and a somatic activation layer (green circles). The activation functions for the respective layers are shown in the insets. The activation of the soma is modeled as simple step function (if the input surpasses a certain threshold, the soma responds). The activation of every separate dendrite branch is modeled as an overlay of a linear response and a (non-linear) step function, to mimic the excitability of dendritic branches. If a dendritic branch is excited (due to a large enough number of same branch active input synapses) it transmits n_{dist}, triggering a somatic response. (H2) The response probability increases as function of the branch length, an effect that becomes more apparent for different increasing numbers of active input synapses S. *: $p<0.05$, **: $p<0.01$, ***: $p<0.001$, ****: $p<0.0001$

Figure 7

Dendritic NMDA-spikes can only be observed in layer 2b neurons

(A) displays a representative layer 2b neuron, (B) a representative layer 2a neuron. (A1/B1) Overlay of electric responses measured at the soma upon electrical stimulation with linear strength increase in layer 1a. (A2/B2) Response to same stimulus after application of APV. (A3/B3) Plot of stimulation strength against area under the curve from the same cell. (A4/B4) Imaged dendritic branch and position of the stimulation electrode. (A5/B5) Fluorescence traces of Ca^{2+} responses at ROIs outlined in A4/B4 under baseline conditions (upper rows, blue and red) and after application of APV (lower rows, black). Increasing stimulation strengths are overlayed. (C1) Area under the curve (AUC) before and after application of APV in layer 2b neurons (blue) and layer 2a neurons (red; layer 2b, pre vs. post: $p<0.05$; layer 2a, pre vs. post: $p=0.18$, paired t test; layer 2a post vs. layer 2b post : $p=0.92$, t-test). (C2) EPSP amplitude

before and after application of APV in layer 2b neurons (blue) and layer 2a neurons (red; layer 2a, pre vs. post: $p<0.05$; layer 2b, pre vs. post: $p=0.7$; paired t test; layer 2a post vs. layer 2b post: $p=0.25$, t-test). (D) Fluorescent Ca^{2+} response before and after application of APV in layer 2b neurons (blue) and layer 2a neurons (red; layer 2b, pre vs. post: $p<0.01$, paired t test; layer 2a, pre vs. post: $p<0.05$, paired t test). *: $p<0.05$, **: $p<0.01$.

,

Figure 8: Nonlinear dendritic integration of glomerular inputs co-determines the onset latency of cortical responses

(A) Comparison of the characteristics of the non-linear (blue lines and symbols) and linear (red lines and symbols) model neuron for the deterministic (noise-less) case. (A1) Voltage traces of a linear (red) and a non-linear (blue) model neuron in response to a regular input spike train with rate R=100 Hz. Vertical black lines show the input spike train. (A2) Response latency for the linear (red) and non-linear (blue) model neuron as function of the input spike rate. For smaller input rates, the latency of the linear model neuron is significantly larger than for the non-linear model neuron. (A3, A4): Raster plots, showing the spike times as function of the input rate for the linear (red and non-linear (blue) model neuron.

Illustrations in B show a comparison of the non-linear and linear model neuron in case in response to noisy input spike trains (Poisson events). (B1) Exemplary voltage trace of a linear model neuron in response to a noisy input spike train with mean rate $\langle R \rangle$=100 Hz. Vertical lines show the input spike train. (B2, B4) Raster plot, showing exemplary response spikes of the linear model neuron (B2) and the non-linear model neuron (B4) in response to noisy input spike trains with mean rate $\langle R \rangle$=100 Hz (orange, blue) and $\langle R \rangle$=150 Hz (red, purple). (B3, B5) Mean population response rate over time in colors corresponding to the results shown in B2 and B4.